

© 2020 by Sun Myung Park. All rights reserved.

ADVANCEMENT AND VERIFICATION OF MOLTRES FOR MOLTEN SALT  
REACTOR SAFETY ANALYSIS

BY

SUN MYUNG PARK

THESIS

Submitted in partial fulfillment of the requirements  
for the degree of Master of Science in Nuclear, Plasma & Radiological Engineering  
in the Graduate College of the  
University of Illinois at Urbana-Champaign, 2020

Urbana, Illinois

Master's Committee:

Assistant Professor Kathryn D. Huff, Advisor  
Associate Professor Tomasz Kozlowski

# Abstract

Molten salt reactors are a class of advanced nuclear reactors that promise numerous improvements over the current fleet of largely light-water reactors. As the world continues its transition towards low-carbon electricity generation to combat climate change, molten salt reactors are potential options in the near-term future for replacing fossil fuel and ageing nuclear power plants. At the current state of development, molten salt reactors still require extensive research to become viable. This thesis presents latest developments in Moltres, a simulation tool for molten salt reactors. These new developments are: support for coupling the incompressible Navier-Stokes and the delayed neutron precursor looping systems, and a new decay heat model for simulating decay heat from fission products at steady state and during transients. This work demonstrates these capabilities in conjunction with existing capabilities through multiphysics simulations of the Molten Salt Fast Reactor concept. This work first verifies the six-group neutron diffusion results from Moltres against continuous-energy Monte Carlo neutron transport results from Serpent 2. The multiplication factors  $k_{\text{eff}}$ , delayed neutron fractions  $\beta$ , temperature reactivity coefficient  $\alpha_T$ , and the six-group neutron energy spectra from Moltres agreed with the high fidelity simulation results from Serpent 2. The  $k_{\text{eff}}$  values have small discrepancies on the order of 100 pcm, which is smaller than some reported literature values. The decay heat model shows an expected flattening of the temperature distribution due to the movement and dispersion of the decay heat precursors throughout the primary coolant loop. This work also demonstrates and verifies steady state and transient multiphysics simulations of the Molten Salt Fast Reactor. The transient scenarios under study are unprotected instances of reactivity insertion, loss of heat sink, loss of flow, and pump overspeed. The steady state and transient results are verified against results from another paper that presented results for the same cases. The steady-state temperature and velocity distributions, and the peak neutron flux showed good agreement with the literature results. Minor differences in the delayed neutron precursor

distribution and the in-core delayed neutron fraction were explainable with the differences in the handling of turbulence in the models. In three of the transient results (reactivity insertion, loss of heat sink, and pump overspeed), Moltres reproduced the expected magnitude and pattern of the reactor response to these transient initiators. The loss of flow results showed greater discrepancies that are attributed to differences in the fluid dynamics modeling in Moltres and the other models. Through the verification studies, this work has also identified avenues for further Moltres software development.

# Acknowledgments

Acks.

# Table of Contents

<b>List of Tables</b> . . . . .	<b>vii</b>
<b>List of Figures</b> . . . . .	<b>viii</b>
<b>Chapter 1 Introduction</b> . . . . .	<b>1</b>
1.1 Background and Motivation . . . . .	1
1.2 Objectives . . . . .	3
1.3 Thesis Outline . . . . .	3
<b>Chapter 2 Molten Salt Reactors</b> . . . . .	<b>4</b>
2.1 History . . . . .	4
2.2 Features . . . . .	6
2.2.1 Safety . . . . .	7
2.2.2 Other Features . . . . .	8
2.3 Literature Review of MSR Simulation Tools . . . . .	9
2.4 Molten Salt Fast Reactor . . . . .	10
2.4.1 Model Reactor Geometry . . . . .	13
2.4.2 Material Specifications . . . . .	14
<b>Chapter 3 Methodology</b> . . . . .	<b>16</b>
3.1 Serpent 2 . . . . .	16
3.2 MOOSE . . . . .	17
3.3 Moltres . . . . .	19
3.4 Modeling Approach . . . . .	19
3.4.1 Central Core Region . . . . .	21
3.4.2 Outer Loop Region . . . . .	28
3.4.3 Flow Transfers . . . . .	30
<b>Chapter 4 Neutronics Results</b> . . . . .	<b>32</b>
4.1 Effective Multiplication Factor and Delayed Neutron Fraction . . . . .	32
4.2 Reactivity Feedback Coefficients . . . . .	34
4.3 Neutron Energy Spectrum . . . . .	34
<b>Chapter 5 Coupled Neutronics/Thermal-Hydraulics Steady-State Results</b> . . . . .	<b>37</b>
5.1 Steady-State Thermal-Hydraulics Results . . . . .	37
5.2 Steady-State Neutronics Results . . . . .	40
5.2.1 Neutron Flux . . . . .	40
5.2.2 Delayed Neutron Fraction . . . . .	40

5.3	Decay Heat . . . . .	45
<b>Chapter 6</b>	<b>Transient Scenarios . . . . .</b>	<b>46</b>
6.1	Unprotected Reactivity Insertion . . . . .	47
6.2	Unprotected Loss of Heat Sink . . . . .	52
6.2.1	Without Decay Heat . . . . .	52
6.2.2	With Decay Heat . . . . .	54
6.3	Unprotected Loss of Flow . . . . .	55
6.4	Unprotected Pump Overspeed . . . . .	60
<b>Chapter 7</b>	<b>Conclusion . . . . .</b>	<b>63</b>
7.1	Future Work . . . . .	64
<b>References</b>	<b>. . . . .</b>	<b>66</b>

# List of Tables

2.1	Main specifications of the Molten Salt Fast Reactor (MSFR) concept [20]. . . . .	11
2.2	Properties of the fuel and blanket salts LiF-AcF <sub>4</sub> . . . . .	15
2.3	Composition (mol %) of the NiCrW Hastelloy. . . . .	15
3.1	Neutron energy group upper bounds used in Serpent 2. . . . .	17
3.2	Decay heat group parameters [9]. . . . .	24
3.3	Boundary conditions in the main reactor geometry (Figure 3.3. . . . .	27
3.4	Boundary conditions in the 1-D outer loop geometry. <i>u</i> represents the 1-D velocity in this region. . . . .	30
4.1	$k_{\text{eff}}$ values from Serpent 2 and Moltres at 973 K. . . . .	33
4.2	$k_{\text{eff}}$ values from Serpent 2 and Moltres at various temperatures from 800 K to 1400 K. . . . .	33
4.3	$\beta_{\text{eff}}$ and $\beta$ values from Serpent 2 and Moltres, respectively, at 973 K. . . . .	34
4.4	Doppler, density, and total temperature coefficients for the temperature range of 800 K to 1400 K. . . . .	34
5.1	Peak neutron flux values from Moltres (this paper), COMSOL [56], and OpenFOAM [10] models along with the temperature distribution with which the values were obtained. . . . .	40
5.2	The fraction of delayed neutrons lost from out-of-core emission and the in-core delayed neutron fraction $\beta_c$ values from Moltres (this paper), and the Polimi and TUDelft models [9]. . . . .	44



# List of Figures

2.1	Schematic view of the MSFR concept. Figure reproduced from Brovchenko et al. [25].	11
2.2	2-D axisymmetric model of the MSFR core used for the simulations in Serpent. All dimensions are in meters. [40]	14
3.1	2-D axisymmetric model of the MSFR. The red box indicates the central core region in the modeling approach in Moltres.	20
3.2	Mesh adopted in Moltres and a close-up view of the mesh around the boron carbide absorber.	23
3.3	The boundaries in the MSFR geometry that are relevant for the boundary conditions mentioned in Table 3.3.	28
4.1	Reactivity values from Serpent and Moltres. The Doppler reactivity values were calculated at a fixed density of $4.1249 \text{ g cm}^{-3}$ . The density reactivity values were calculated at a fixed temperature of 973 K.	35
4.2	The fine-group and six-group neutron energy spectra from Serpent 2 and Moltres normalized per unit lethargy.	35
5.1	Temperature and velocity fields in the core from Moltres (left), Polimi (center), and TUDelft (right) models. The colors represent temperature according to the respective colorbars and the arrows represent velocity fields.	38
5.2	Fuel salt flow streamlines and velocity magnitude in the core. The colors represent velocity magnitude according to the colorbar on the right.	38
5.3	Neutron flux distributions in the core for neutron energy groups 1 to 6. The y and x axes represent height and radius (in cm) of the core relative to the entire reactor geometry.	41
5.4	Axial (left) and radial (right) neutron flux distributions in the core for neutron energy groups 1 to 6.	42
5.5	delayed neutron precursor (DNP) distributions in the core for DNP groups 1 to 8 (from left to right, top to bottom). Refer to Figure 5.3 for the height and radius scales on the y and x axes, respectively. Note the different scales for each distribution.	42
5.6	Total delayed neutron source distribution in the core from Moltres (left), Polimi (center), and TUDelft (right) models.	43
6.1	Power output following a 50 pcm step-wise reactivity insertion in the Moltres, Polimi, and TUDelft models [9].	48
6.2	Average core temperature increase following a 50 pcm step-wise reactivity insertion in the Moltres, Polimi, and TUDelft models [9].	48

6.3	Power output during the prompt response following a 50 pcm step-wise reactivity insertion in the Moltres, Polimi, and TUDelft models [9]. . . . .	49
6.4	Power output following a 200 pcm step-wise reactivity insertion in the Moltres, Polimi, and TUDelft models [9]. . . . .	50
6.5	Average core temperature increase following a 200 pcm step-wise reactivity insertion in the Moltres, Polimi, and TUDelft models [9]. . . . .	50
6.6	Power output during an unprotected loss of heat sink transient in the Moltres, Polimi, and TUDelft models [9] without decay heat. . . . .	53
6.7	Average core temperature increase during an unprotected loss of heat sink transient in the Moltres, Polimi, and TUDelft models [9] without decay heat. . . . .	53
6.8	The change in flow rate in the Polimi and TUDelft models and the imposed flow rate in Moltres. . . . .	55
6.9	Power output during an unprotected loss of flow transient in the Moltres, Polimi, and TUDelft models [9]. . . . .	58
6.10	Average core temperature increase during an unprotected loss of flow transient in the Moltres, Polimi, and TUDelft models [9]. . . . .	58
6.11	Temperature and velocity fields in the core at $t = 300$ s during a loss of flow transient in the Moltres ( $\mu_c = \frac{1}{2}\mu_{t,0}$ ), Polimi, and TUDelft models. . . . .	59
6.12	Power output during an unprotected pump overspeed transient in the Moltres, Polimi, and TUDelft models [9]. . . . .	61
6.13	Average core temperature increase during an unprotected pump overspeed transient in the Moltres, Polimi, and TUDelft models [9]. . . . .	61
6.14	The first 20 s of the power output and average core temperature increase during an unprotected pump overspeed transient. . . . .	62

# Chapter 1

## Introduction

### 1.1 Background and Motivation

Greenhouse gas emission from human activities is the main cause of climate change, a global phenomenon characterized by shifting weather patterns and rising temperatures. The concentration of CO<sub>2</sub>, a greenhouse gas, in the atmosphere has been rising steadily throughout modern human history [1]. Climate change has dire consequences on human health and safety due to extreme weather events and the overall impact on food production [2]. As a result, urgent measures are necessary to limit greenhouse gas emissions, namely CO<sub>2</sub> emissions from electricity generation.

Electricity generation from burning fossil fuels represents the greatest source of CO<sub>2</sub> emissions (38% in 2018 [3]); replacing it with low-carbon alternatives would curb a significant fraction of emissions. Nuclear power is a viable low-carbon replacement for burning fossil fuels. Other low-carbon energy sources include solar-, wind-, and hydro-power. Each energy source has its own set of advantages and disadvantages; nuclear power's advantage over renewable energy sources is that it provides consistent base-load power independent of weather and geographical location [4]. Employing a diverse mix of these energy sources ensures energy security and reliability in our transition towards a low-carbon future [4].

The world would have to ramp up the current rate of reactor deployments to displace some of the presently large share of energy production from fossil fuel power plants. However, several obstacles stand in the way of mass reactor deployments. These obstacles include perceived safety risks, sustainability concerns, nuclear proliferation risks, and the ability to compete economically with other sources of energy [5]. A potential solution to the aforementioned issues is the Molten Salt Reactor (MSR) concept, one of six advanced reactor designs selected by the Generation IV International Forum [6] for continued research and development.

The primary coolants in MSR's consist of a molten salt mixture with fissile and/or fertile material directly dissolved in the coolant. MSR's possess an inherently robust safety feature in the strongly negative fuel temperature coefficient of reactivity. Some designs can also incorporate the thorium fuel cycle for improved sustainability arising from the use of abundant natural thorium resources and reduced transuranic waste. The latter also reduces economical costs associated with long-term nuclear waste storage. In addition, the ability to operate at near atmospheric pressures eliminates the need for a thick pressure vessel and drives down construction costs, while online fuel reprocessing reduces reactor downtime during reactor operation.

However, the liquid fuel form also brings about novel computational challenges in simulating the transient behavior of MSR's; the interactions between neutronics and thermal-hydraulics are stronger due to greater fuel material expansion. Furthermore, delayed neutron precursors (DNPs) in MSR's can flow freely within the primary coolant loop as opposed to being held in place in a solid fuel matrix. Therefore, the choice of coupling methods for each set of physics requires careful consideration.

Most reactor analysis applications are usually reactor-specific by design such as PARCS and TRACE for Light Water Reactors (LWR's), and SAS4A/SASSYS-1 for liquid metal cooled reactors. Thus, these applications would disregard MSR-specific phenomena and are inappropriate for MSR analysis without any modifications to the source code. Some research efforts do focus on adapting these applications for MSR analysis. Examples include the coupling of modified versions of TRACE and PARCS [7], and the development of VERA-MSR from the integrated LWR simulation tool VERA [8]. Others developed their MSR simulation tools from general multiphysics or Computational Fluid Dynamics (CFD) applications such as COMSOL [9] and OpenFOAM [10].

Moltres is an open source MSR simulation tool that falls under the latter category [11]. It is an application built in the Multiphysics Object-Oriented Simulation Environment (MOOSE) [12] parallel finite element framework. Lindsay et al. first presented the tool in 2017 and demonstrated its capabilities by simulating 2-D and 3-D models of the Molten Salt Reactor Experiment (MSRE) [11]. The results showed good qualitative agreement with the original design calculations by MSRE researchers at Oak Ridge National Laboratory (ORNL). There has since been new developments in Moltres allowing for more accurate MSR simulations.

## 1.2 Objectives

This thesis demonstrates latest capabilities of Moltres [11], an open source MSR simulation tool. In particular, this thesis presents two more recent developments in Moltres, namely fully integrating MOOSE’s incompressible Navier-Stokes module into Moltres, and introducing a decay heat model. The main objective of this thesis is to verify Moltres’ latest capabilities in modeling multiphysics, steady-state, and transient behavior of fast-spectrum MSRs through the study of the Molten Salt Fast Reactor (MSFR) concept. Code-to-code verification is an important exercise in software development for ensuring that the application produces accurate and reliable results. This thesis covers the MSFR concept mainly because it has been studied extensively with readily available literature data to verify our results against. The steady-state and transient results also feature a significant degree of physics interaction between the neutronics and thermal-hydraulics. This present work will first present a verification of Moltres’ MSFR neutronics results against Serpent 2, followed by a verification of the coupled neutronics/thermal-hydraulics steady-state and transient accident results against results from the Polimi and TUDelft models published by Fiorina et al. [9]. The secondary objective is to identify areas of improvement in Moltres for future research.

## 1.3 Thesis Outline

The outline of this thesis is as follows. Chapter 2 discusses the history and features of MSRs, and a literature review of existing MSR simulation tools. The chapter also covers the MSFR concept in greater detail. Chapter 3 details the software and the general modeling approach for generating the results in this thesis. Chapter 4 provides a neutronics assessment by comparing key neutronics parameters from Moltres’ eigenvalue calculations to Serpent’s Monte Carlo calculations. Chapter 5 presents steady-state results of coupled neutronics/thermal-hydraulics MSFR simulations in Moltres. Chapter 6 presents transient accident simulation results for unprotected reactivity insertions, unprotected loss of heat sink, unprotected loss of flow, and unprotected pump overspeed, respectively. Lastly, Chapter 7 summarizes the key findings in this thesis and posits some potential avenues for future work.

## Chapter 2

# Molten Salt Reactors

MSRs are one of six advanced reactor designs shortlisted by the Generation IV Forum in 2001 for promising significant advances in safety, sustainability, efficiency, and cost over existing designs. This has attracted significant attention and resources towards MSR research, most noticeable by the number of start-up companies that have emerged in recent years touting various MSR designs. This chapter provides a brief history of MSRs, followed by the distinctive features that earned the concept the label of being a Generation IV reactor. Lastly, this chapter presents the reference specifications of the MSFR concept studied in this work.

### 2.1 History

The first MSR, named the Aircraft Reactor Experiment (ARE), dates back to the 1940s as part of the US Aircraft Nuclear Propulsion program [13]. Researchers recommended the molten fluoride salts in particular for high uranium solubility, chemical stability, low vapor pressure even at high temperatures, decent heat transfer properties, resistance against radiation damage, and reduced corrosive effects on some common structural material [13]. They subsequently built the 2.5 MW<sub>th</sub> ARE reactor at ORNL, where it achieved criticality on November 1954 and generated 100 MWh over nine days. The fuel consisted of enriched uranium in a molten salt mixture of NaF, ZrF<sub>4</sub>, and UF<sub>4</sub>. Additionally, the reactor used blocks of BeO for neutron moderation. The aircraft program ultimately never came to fruition as the development of intercontinental ballistic missiles effectively eliminated the need for long-range nuclear-powered bomber aircraft.

However, the successful demonstration of the ARE spurred further research into adapting MSRs for civilian power generation [13]. One key finding from the research was that the thorium fuel cycle had a better breeding ratio than the <sup>238</sup>U-to-<sup>239</sup>Pu fuel cycle in thermal-spectrum reactors.

Ultimately, these efforts culminated in the design, construction, and successful operation of the MSRE, a graphite-moderated thermal MSR. The MSRE had a graphite-moderated design with a LiF-BeF<sub>2</sub>-ZrF<sub>4</sub>-UF<sub>4</sub> fuel salt mixture, initially rated at 10 MW<sub>th</sub> but later restricted to 8 MW<sub>th</sub> due to a miscalculation of heat transfer capabilities [14]. In January 1969, the MSRE became the first reactor to run on <sup>233</sup>U fuel.

Building on their experience with the MSRE, ORNL proposed a new program for the construction and operation of a demonstration reactor based on the Molten Salt Breeder Reactor (MSBR) concept that they had developed [15]. The MSBR is a thermal-spectrum, single fluid reactor with fertile <sup>232</sup>Th isotopes mixed directly into the FLiBe molten salt for <sup>233</sup>U breeding [16]. Like the MSRE, the MSBR relies on continuous online reprocessing to add fertile material and remove fission product neutron poisons. Researchers estimated the doubling time (the minimum amount of time required to produce enough fissile material to start up another MSBR) to be approximately 22 years. However, ORNL failed to secure funding for the new program in their two attempts in 1972 and 1974. Nevertheless, from a technical perspective, two independent technology evaluation and design studies of the MSR had reported favorably on the promise of the system [15].

In spite of this setback, research into MSRs continued through the late 1970s. In 1980, ORNL published a report describing a new MSR concept, called the Denatured Molten Salt Reactor (DMSR) [16] with denatured <sup>235</sup>U fuel (i.e. low-enriched uranium). The ORNL researchers developed this design in response to the fuel reprocessing restrictions introduced by President Ford in 1976. The DMSR would operate as a once-through converter system without fuel reprocessing. While the fuel consists of 19.75 % high-assay low-enriched uranium, the initial core loading includes thorium to boost its conversion ratio throughout its lifetime. It has a continuous online feed consisting of high-assay low-enriched uranium (HALEU) to maintain criticality, and denatured <sup>235</sup>U to keep uranium enrichment levels below nuclear non-proliferation policy thresholds. The design also includes a gas sparging system for removing gaseous fission products, while noble metals plate out onto the walls of the coolant loop. The older MSBR design had a significant drawback; the extensive neutron damage in the graphite moderator necessitated frequent replacement (every four years) throughout its operational lifetime. The DMSR avoids this issue by having a lower power density while maintaining the overall power output of 2250 MW<sub>th</sub>. As a result, researchers projected that

the graphite moderator would last for the entirety of the DMSR's design lifetime.

There was a concurrent program at the UK Atomic Energy Authority for the development of a 2500 MW<sub>e</sub> lead-cooled Molten Chloride Fast Reactor concept [17]. It is a dual fluid system, with separate loops for the fuel salt and the blanket salt. The blanket is a 1 m-wide tank surrounding the core. The absence of moderators and the choice of chloride over fluoride salt resulted in a relatively hard neutron spectrum which favors <sup>239</sup>Pu breeding over the thorium cycle. The UK researchers performed some experiments to study molten salt chemistry but there were no reactor prototypes. The UK program eventually shut down just like its US counterpart partly due to the successful demonstration of the Prototype Fast Reactor which had achieved criticality in 1974.

Following a lull lasting through the late 20th century, MSR research picked up pace due to renewed interest initiated by the Generation IV Forum in 2001. Today, various national and commercial bodies are developing numerous MSR concepts.

## 2.2 Features

As mentioned in Chapter 1, the most significant difference between MSRs and other reactor concepts is the liquid fuel in MSRs; fissile and/or fertile material is dissolved in high temperature, commonly eutectic mixtures of molten salts. Molten salt-cooled, solid-fuel reactors also exist but this thesis will focus on liquid-fuel reactors. The primary coolant loop containing the fuel salt transfers heat through a heat exchanger to the clean, intermediate loop. The liquid fuel form allows for continuous online fuel reprocessing, and the removal of gaseous fission products via a gas sparging system.

The various MSR designs under development today illustrate the flexibility of this reactor concept. Graphite-moderated thermal-spectrum MSRs are typically straightforward low-enriched uranium (LEU) burners or <sup>232</sup>Th/<sup>233</sup>U iso-breeders/breeders, while epithermal- and fast-spectrum MSRs can operate as transuranic (TRU) fuel burners or <sup>238</sup>U/<sup>239</sup>Pu breeders. Breeder designs can be further categorized into one- or two-fluid designs. Two-fluid designs feature separate blanket molten salt mixtures that contain higher proportions of fertile material than the fuel salt mixture. Examples of one-fluid designs include the Integral Molten Salt Reactor from Terrestrial Energy [18] and the MSR design from Transatomic Power [19] while two-fluid designs include the MSFR [20] and Molten Salt Actinide Recycler and Transmuter (MOSART) [21].



### 2.2.1 Safety

MSRs rely on natural physical phenomena for passive safety such as the strong negative temperature reactivity feedback of the fuel salt due to greater temperature-induced expansion in liquid fuel than solid fuel. Combined with the Doppler broadening of resonance capture cross sections present in both fuel forms, there would be a smaller temperature increase following an unprotected reactivity insertion. The overall temperature reactivity coefficient varies widely among MSR designs due to other structures, such as moderators and reflectors, present in the core. In particular, graphite moderators tend to have slightly positive temperature reactivity coefficients. The MSBR concept has this issue, but the total temperature reactivity coefficient is still relatively large and negative [22]. The negative temperature reactivity feedback provides a great degree of control and stability as it is always present in an MSR regardless of the operating conditions.

Continuous online fuel reprocessing allows operators to maintain low excess reactivity inventories in the core as additional fuel can be added on an ad hoc basis. Reprocessing and gas sparging systems help reduce fissile requirements by continuously removing neutron poisons. These factors, in addition to the strong negative temperature reactivity coefficient, diminish the likelihood and severity of unprotected criticality accidents in MSRs [23]. In the unlikely situation in which an MSR encounters a severe runaway reaction, MSRs rely on another passive safety feature: freeze plugs. Various freeze plugs designs exist for different MSRs. The freeze plug in the MSFR concept is a plug of solidified salt at the bottom of the core actively cooled by fans or other cooling systems to keep its temperature just below the freezing point of the salt [24]. When temperatures in the core exceed a certain threshold during a dangerous transient, the freeze plug melts and drains the molten salt into a containment tank designed to keep the salt in a subcritical configuration. This is especially easy to achieve in thermal-spectrum MSRs as the absence of moderators in the containment tank would automatically drive the multiplication factor down below unity [23].

During pump failure accidents, natural circulation can passively sustain enough heat transfer to remove decay heat and prevent catastrophic structural failure. If natural circulation proves insufficient, the aforementioned freeze plug can drain the salt out of the core. Decay heat in MSRs with online reprocessing is typically lower than that in LWRs due to the continuous removal of fission products. For example, the decay heat in an MSFR after reaching equilibrium salt composition is

approximately 3.5% of full reactor power compared to 6% in LWRs [25].

MSRs also typically have a high margin to boiling under nominal operating conditions so that fuel salt boiling is absent [23]. Furthermore, the reactor vessel is consequently subject to much lower stresses as MSRs operate at near-atmospheric pressure levels. Thus, the probability of pipe ruptures due to high pressure is low.

However, MSRs do have some associated safety risks. Firstly, MSRs have smaller fractions of delayed neutron precursors in the active core region as some of them decay in the external loop regions. This complicates reactor control and may result in faster transients due to the decrease in average neutron lifetime. Secondly, hot molten salts are corrosive and the corrosion mechanism is different from conventional corrosion induced by water and other common agents [26]. The intense gamma and neutron radiation in the core may also accelerate corrosion in the structural components. Lastly, overcooling in pipes and heat exchangers may pose operational challenges as the salt can freeze and restrict flow, causing a loss of flow accident [27].

### 2.2.2 Other Features

MSRs have several positive sustainability features. The continuous removal of neutron poisons by the online reprocessing and gas sparging systems creates good neutron economy in MSRs [28]. Both  $^{232}\text{Th}/^{233}\text{U}$  and  $^{238}\text{U}/^{239}\text{Pu}$  fuel cycles are viable candidates for breeding in MSRs, with the former being more suited for thermal reactors and the latter being more suited for fast reactors.

The  $^{232}\text{Th}/^{233}\text{U}$  fuel cycle produces significantly less TRU waste than the other cycles due to the smaller atomic masses of  $^{232}\text{Th}$  and  $^{233}\text{U}$ . This reduces the overall radiotoxicity and long-term decay heat associated with long-lived plutonium and minor actinide (MA) isotopes. The combination of TRU fuel and  $^{232}\text{Th}$  feed in fast spectrum MSRs contributes to lower levels of TRU waste going into long-term storage in nuclear waste repositories [29].

Nuclear non-proliferation concerns in thorium-fueled MSRs involve the separation of the intermediate  $^{233}\text{Pa}$  isotope from the fuel salt.  $^{233}\text{Pa}$  decays into  $^{233}\text{U}$  with a half-life of approximately 27 days and the  $^{233}\text{U}$  produced is equivalent in potency to  $^{239}\text{Pu}$  for nuclear weapons production [30]. The highly radioactive  $^{232}\text{U}$  by-product provides some level of proliferation resistance but nuclear proliferators can sidestep this complication; they can separate the  $^{232}\text{U}$  away from the combined

$^{232}\text{Pa}/^{233}\text{Pa}$  stream after most of the  $^{232}\text{Pa}$  has decayed into  $^{232}\text{U}$  at a short half-life of 1.31 days [30]. Safeguards by design and close monitoring of MSR are therefore essential to avoiding spent nuclear fuel diversion.

Economic analyses of MSRs are preliminary at the current stage of MSR development. Qualitatively, many technical factors favor MSRs over LWRs. Some of these factors include: smaller reactor core size due to low operating pressures, higher thermal efficiency and cheaper air-cooling systems due to high operating temperatures, reduction in fuel fabrication costs, and shorter reactor shutdown periods due to online refueling [31]. Moir [32] published data from ORNL reports on the estimated electricity costs for a 1000 MWe MSR with 20% enriched  $^{235}\text{U}$  fuel and no reprocessing throughout the reactor's 30-year lifetime. Adjusted to year 2000 dollars, the electricity costs for this type of MSR was 7% and 8% lower than that of pressurized water reactors and coal power plants. These differences are within the  $\pm 10\%$  uncertainty range but Moir remains optimistic. The author also notes that costs could be lower in an MSR with fertile feed and online reprocessing could reach fuel self sufficiency.

In terms of technological readiness, MSRs still require significant research efforts and engineering demonstrations for experimental validation of various components before a full commercial model can be commissioned. Work towards creating a safety and licensing framework for MSRs has picked up pace only in recent years due to the growing interest from commercial MSR developers.

## 2.3 Literature Review of MSR Simulation Tools

In the past two decades, researchers have developed several new tools for simulating steady-state and transient behavior in MSRs. Many of the earlier efforts featured simplifications in simulating thermal-hydraulics by solving 1-D Navier-Stokes equations or using predetermined uniform velocity fields [33, 34]. In more recent years, there has been significant progress towards fully coupled, spatial codes that feature 2-D axisymmetric or full 3-D models. In 2011, Cammi et al. [35] performed a "Multi-Physics Modelling (MPM)" analysis of a simplified 2-D axisymmetric model of a single MSBR fuel channel using the commercial finite element analysis software COMSOL Multiphysics. The physics were implemented through the two-group neutron diffusion equations, and the Reynolds-averaged Navier-Stokes (RANS) standard  $k$ - $\epsilon$  turbulence model, for the neutronics

and thermal-hydraulics respectively. The authors emphasized the need for proper full coupling of the multiphysics and presented both steady-state and transient results in various scenarios such as reactivity insertions, changes in pumping rate, and the presence of periodic perturbations. This approach was featured again in a later paper by Fiorina et al. [9] in 2014 for a 2-D axisymmetric model of the MSFR. The authors presented results from the Politecnico di Milano COMSOL-based approach, and another approach by researchers from Delft University of Technology, in which they coupled their in-house neutronics and thermal-hydraulics codes, DALTON and HEAT respectively. With multigroup neutron diffusion and RANS formulations on ultra fine meshes, both models agreed on the steady-state neutron flux, temperature, and DNP distributions, as well as the power responses following various accident transient initiations. Aufiero et al. [10] concurrently developed a full-core 3-D model of the MSFR on OpenFOAM, albeit with one-group neutron diffusion to reduce computational load. With the 3-D model, the authors could simulate the asymmetric reactor response to the failure of a single pump in the sixteen-pump MSFR configuration. The authors also provided quantitative data supporting the use of implicit coupling over explicit coupling to obtain accurate solutions of the transient cases. Recognizing the huge computational burden required for full 3-D simulations, later authors came up with innovative ways to alleviate this issue. Methods include selective geometrical reduced order modeling for various components of a reactor based on the importance of the physical phenomena being simulated [36], or using a novel, efficient method for neutronics calculations [37].

## 2.4 Molten Salt Fast Reactor

The MSFR is a European reference fast-spectrum MSR concept [38, 39]. Table 2.1 and Figure 2.1 show the main specifications and schematic view of the MSFR, respectively. Developed from the MSBR design, the MSFR is intended to run primarily on a closed thorium fuel cycle with continuous online fuel reprocessing. Several reasons motivated the omission of graphite moderators from the original MSBR design. Graphite is susceptible to long-term radiation damage and replacement is likely to be necessary during the operating lifetime of the reactor. Graphite also has a positive temperature coefficient of reactivity; eliminating graphite from the design ensures a greater safety margin [38]. While negative temperature coefficients are attainable with very thermalized spectra,

breeding ratios deteriorated significantly due to parasitic absorption in the graphite [38].

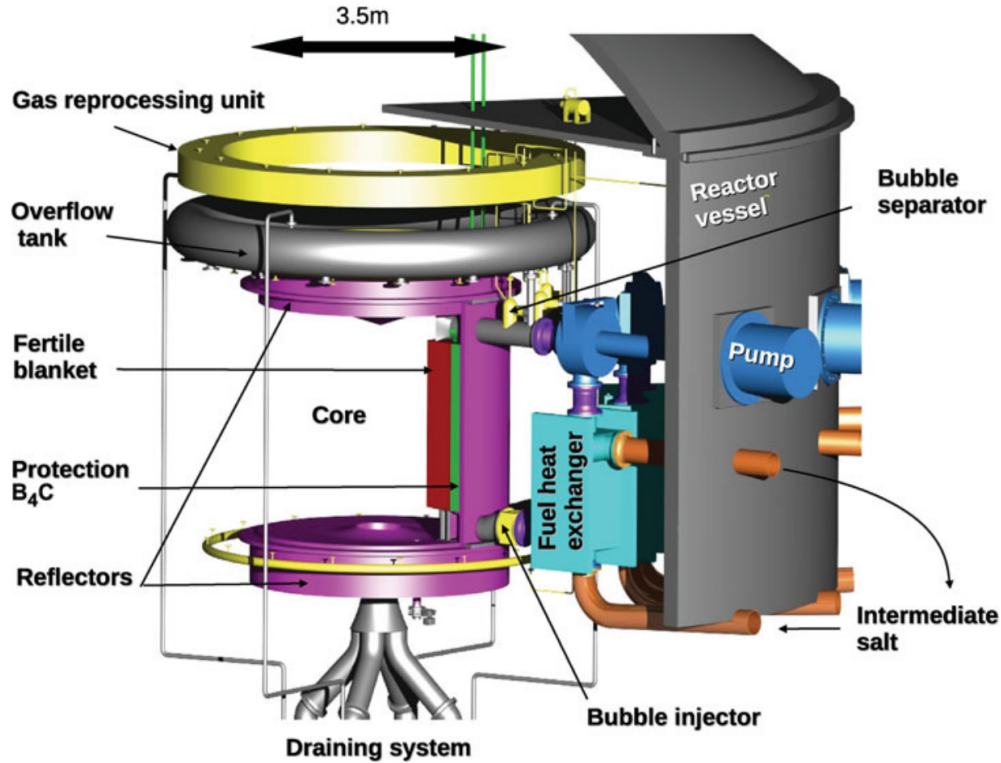


Figure 2.1: Schematic view of the MSFR concept. Figure reproduced from Brovchenko et al. [25].

Table 2.1: Main specifications of the MSFR concept [20].

Parameter	Value
Thermal/Electric output [ $\text{MW}_{\text{th}}/\text{MW}_{\text{e}}$ ]	3000 / 1500
Salt volume [ $\text{m}^3$ ]	18
Salt fraction in core	0.5
Number of circulation loops	16
Nominal flow rate [ $\text{kg s}^{-1}$ ]	18500
Nominal circulation time [s]	4.0
Inlet/outlet temperature [K]	923 / 1023
Blanket volume [ $\text{m}^3$ ]	7.3

In the MSFR design, fuel salt flows vertically upward through a  $9 \text{ m}^3$  central core region. At the top of the core, the flow separates into sixteen smaller external loops, each of which passes through a heat exchanger before being pumped back into the bottom of the core. The salt also passes through the online salt reprocessing and gas sparging systems located along the external loops. A toroidal blanket tank containing fertile salt for breeding surrounds the core radially. The top and bottom of the core are enclosed by nickel alloy reflectors. A layer of boron carbide behind

the blanket tanks protects the peripheral equipment from excessive neutron damage. During severe accidents when core temperatures rise to dangerous levels, the actively fan-cooled freeze plug at the bottom of the core melts and drains the fuel salt into a containment vessel designed to keep the salt subcritical.

Although the MSFR is primarily designed to operate on the thorium fuel cycle, it supports a range of start-up fuel and feed compositions. This versatility is particularly important for the first few MSFRs to be deployed due to the lack of  $^{233}\text{U}$  reserves required for the initial core loading. In general, the fuel and blanket salts are approximately composed of eutectic mixtures of 77.5% LiF - 22.5% AcF<sub>4</sub>; AcF<sub>4</sub> represents actinide fluorides such as uranium, thorium, plutonium, and other TRU fluorides. For an initial composition consisting of  $^{232}\text{Th}$  and  $^{233}\text{U}$ , the benchmark value for the amount of  $^{233}\text{U}$  for criticality under normal operating conditions is 2.5 mol%. However, a neutronic benchmark study by Brovchenko et al. [40] shows that different neutronics software with different nuclear data clearly provide different  $k_{eff}$  estimates even with the same isotopic compositions and temperature distributions. The individual co-authors adjusted the ratio of  $^{232}\text{Th}$  to  $^{233}\text{U}$  slightly to achieve exact criticality at a uniform temperature of 973 K for their own neutronics software [40]. This thesis performs the same exercise to adjust the inlet and outlet temperatures to match nominal values.

The thermal and electric power output of the MSFR are 3000 MW<sub>th</sub> and 1500 MW<sub>e</sub>, respectively. The high thermal efficiency ( $\eta_{th} = 0.5$ ) is due to the high operating temperature. The inlet and outlet temperature specifications of the fuel salt are 923 K and 1023 K, respectively, for a minimum 50 K temperature buffer between the operating temperatures and the melting point of the salt (873 K) [41]. The MSFR has heat exchangers and an intermediate coolant loop to isolate the power conversion system from the highly radioactive fuel salt. This also serves as a layer of containment between the radioactive material and the outside environment. The exact composition of the intermediate coolant is not finalized yet but potential candidates include NaF-NaBF<sub>4</sub>, FLiNaK, LiF-ZrF<sub>4</sub>, and FLiBe [42].

### 2.4.1 Model Reactor Geometry

This present work uses the same 2-D square-cylindrical MSFR design to benchmark our results against results published by Fiorina et al. [9]. The design is a 2-D axisymmetric representation of the MSFR with the sixteen individual external loops homogenized into a single outer loop as shown in Figure 2.2. For the multigroup group constants calculations in Serpent, the 2-D axisymmetric model is extended into a 3-D model by a 360-degree rotation about the central axis. The material definitions are the same as those specified in the reference MSFR model. Accordingly, the pump and heat exchanger regions are assumed to be composed of 100% fuel salt. While this may not be entirely accurate, the exact details of the pump and heat exchanger systems are still under active study, and this external loop region is presumed to be of little neutronic importance due to its position behind the strong boron carbide neutron absorber layer.

Although this present work uses the same 2-D axisymmetric geometry for generating group constant data from Serpent, there are two minor differences between the MSFR geometry used in the Moltres model, and the Polimi and TUDelft models [9]. Firstly, the reactor geometry for Moltres excludes the 2-cm-thick structural material around the blanket tank that separates the fuel and blanket salts. The thickness is much smaller than the rest of the regions in the geometry and caused issues for meshing. The neutronics results in Chapter 4 shows that the overall  $k_{eff}$  and other parameters from Moltres show good agreement with that from Serpent. It also has no direct impact on the temperature distribution results because this present work solves for the temperature distribution in the primary loop with homogeneous Neumann boundary conditions on the fuel salt-to-wall interface. This approach is for consistency with the Polimi and TUDelft models.

The second difference pertains to the out-of-core section of the primary loop. The focus for Moltres development has been on core multiphysics over detailed out-of-core multiphysics. The Moltres model simulates the outer loop as a 1-D pipe with a pointwise heat sink to represent the heat exchanger. To simulate the pumps, a Dirichlet boundary condition for velocity at the inlet boundaries drives the flow in the central core region of the primary loop. At every timestep, Moltres converges the core and outer loop calculations using Picard iterations. This approach shares some similarities with the geometric multiscale modeling approach by Zanetti et al. [36]. Future models could create a better representation of the primary loop by implementing a whole continuous loop

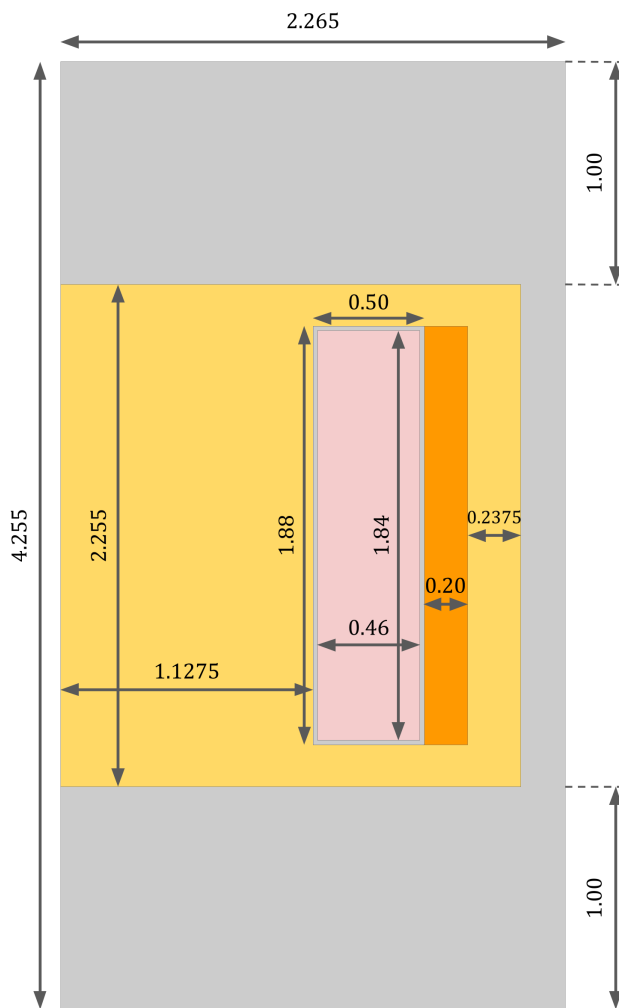


Figure 2.2: 2-D axisymmetric model of the MSFR core used for the simulations in Serpent. All dimensions are in meters. [40]

with pressure increases and drops corresponding to the pumps and heat exchangers.

## 2.4.2 Material Specifications

This section details the material specifications of the various reactor components in the MSFR.

### Molten Salt

The reference start-up salt composition for the fuel and blanket salts is 77.5% LiF - 22.5% AcF<sub>4</sub> (actinide fluorides) [29]. Typically, researchers working with the MSFR model tweak the exact



actinide composition by varying the  $^{232}\text{Th}$  to  $^{233}\text{U}$  ratio to obtain a  $k_{\text{eff}}$  value of 1 at a uniform temperature of 973 K [40]. Thus, the exact actinide compositions vary depending on the nuclear data library and neutron transport code. This present work uses a fuel salt composition of 77.5% LiF - 19.913% ThF<sub>4</sub> - 2.587%  $^{233}\text{UF}_4$  for all calculations, which is a simplifying assumption but a fuel burnup analysis is complex and out of scope for this thesis. Table 2.2 shows relevant physical properties of the fuel and blanket salts.

Table 2.2: Properties of the fuel and blanket salts LiF-AcF<sub>4</sub>.

Property	Formula	Value at 973 K	Validity Range
Melting temperature [K]	841	N/A	1 bar
Boiling temperature [K]	1874	N/A	1 bar
Density, $\rho$ [kg m <sup>-3</sup> ]	$4094 - 0.882 \cdot (T - 1008)$	4125	893-1123 K
Dynamic viscosity, $\mu$ [Pa s]	$\rho \cdot 5.55 \times 10^{-8} \cdot e^{3689/T}$	1.015	898-1121 K
Thermal conductivity, $k$ [W m <sup>-1</sup> K <sup>-1</sup> ]	$0.928 + 8.397 \times 10^{-5} \cdot T$	0.01010	891-1020 K
Specific heat, $c_p$ [J kg <sup>-1</sup> K <sup>-1</sup> ]	$-1111 + 2.78 \cdot T$	1594	867-907 K

## Structural Materials

The reflectors on the periphery of the reactor core and the blanket tank are made of a NiCrW Hastelloy (metal alloy) [40]. Table 2.3 details the elemental composition of the Hastelloy. The alloy has a density of 10 g·cm<sup>-3</sup>. The MSFR also includes a 20 cm layer of boron carbide (B<sub>4</sub>C) to protect the heat exchangers and pumps from neutron irradiation. The reference specifications indicate that natural boron is used, which is composed of 19.8 %  $^{10}\text{B}$  and 80.2 %  $^{11}\text{B}$ , with an overall density of 2.52 g·cm<sup>-3</sup>.

Table 2.3: Composition (mol %) of the NiCrW Hastelloy.

Ni	W	Cr	Mo	Fe	Ti	C	Mn	Si	Al	B	P	S
79.432	9.976	8.014	0.736	0.632	0.295	0.294	0.257	0.252	0.052	0.033	0.023	0.004

# Chapter 3

## Methodology

This work demonstrates the MSFR simulation capabilities of Moltres, a multiphysics simulation tool for MSRs [11]. To run simulations on Moltres, it requires input group constant data from a neutron transport solver for the multigroup neutron diffusion calculations, and a mesh file representing the geometry of the reactor. This work uses Serpent 2 [43] for the former and Trelis [44] for the latter. This chapter provides brief introductions to Serpent 2, MOOSE, and Moltres, and the modeling approach for the multiphysics simulations in Moltres.

### 3.1 Serpent 2

Serpent 2 [43] is a continuous-energy Monte Carlo neutron transport application under active development led by the VTT Technical Research Centre of Finland. It was created in 2004 for group constant generation in lattice geometries, and has since grown to support more general capabilities. Serpent 2 is highly parallelizable, supporting both MPI and OpenMP parallel programming APIs. It has also been validated and verified against experimental data and other well-established codes.

In Serpent 2, each neutron is tracked through a combination of ray-tracing-based surface tracking and rejection sampling-based delta tracking. Users may define the number of neutron histories and the number of active and inactive cycles for each simulation. Inactive cycles are required for fission source distribution convergence, before interactions are tallied in the active cycles. Interaction types and locations are determined stochastically based on neutron interaction data from established nuclear data libraries (e.g. ENDF [45], JEFF [46]). These nuclear data libraries provide continuous-energy cross section data at discrete temperatures. Beyond the discrete library temperatures, Serpent 2 has a built-in Doppler-broadening preprocessor that extrapolates the relevant cross section data from a lower temperature [43].

In the context of this work, Serpent 2 uses the JEFF-3.1.2 nuclear data library [46] to generate group constants needed by Moltres. The relevant group constant data are collapsed into six neutron energy groups, and calculated at discrete temperature values from 800 K to 1300 K at 100 K intervals. Table 3.1 shows the upper bounds of each neutron energy group. The group constants relevant for neutronics calculations in Moltres are the macroscopic fission  $\Sigma_g^f$ , removal  $\Sigma_g^r$ , and scattering  $\Sigma_{g' \rightarrow g}^s$  neutron cross sections, neutron diffusion coefficients  $D_g$ , average fission energies  $\epsilon_g$ , average neutron yields  $\nu$ , inverse neutron speeds  $1/v$ , flux spectra  $\chi$ , DNP decay constants  $\lambda_i$ , and effective delayed neutron fractions  $\beta_{eff}$ . These group constants are extracted from the Serpent 2 output files using a Python script available from the Github repository that holds the Moltres source code [47]. The script rewrites the group constants into a Moltres-compatible format.

Serpent 2 provides standard geometric surfaces (e.g. planes, cylinders, cones) for defining reactor geometries. In this work, the reactor geometry is the same axisymmetric MSFR geometry from the paper by Fiorina et al. [9], as shown in Fig. 2.2.

Table 3.1: Neutron energy group upper bounds used in Serpent 2.

Group number	Upper bound [MeV]
1	20
2	2.2313
3	0.4979
4	0.024 787 5
5	0.005 530 8
6	0.000 748 5

## 3.2 MOOSE

MOOSE [12] is a highly parallelizable, finite element framework developed at Idaho National Laboratory (INL) for simplifying the process of creating fully-coupled, non-linear, multiphysics solvers. The framework provides a user-friendly interface for this task through object-oriented programming in C++. All aspects of a typical multiphysics problem, such as the terms in the partial differential equations (PDEs), the initial and boundary conditions, the material properties, etc., are represented in MOOSE as C++ objects. New objects can inherit properties from related old objects to simplify implementation and reduce code duplication. These objects are commonly

referred to as kernels in MOOSE. Overall, this approach is helpful for many researchers, a significant fraction of whom do not possess high-level programming backgrounds, as they are unencumbered by the technical details and complexities involved in programming mesh handling and PDE solving in finite element analysis.

MOOSE itself relies on libMesh [48] and PETSc [49] for its mesh handling and PDE solver functionalities. As a result, MOOSE supports adaptive meshing schemes and automatic variable scaling amongst other advanced features for improved accuracy and performance times. Full coupling is maintained by the execution of Newton-based solves on the weak formulations of the multiple PDEs to minimize the residual values. Fully-coupled solves are essential for accurately resolving systems with strongly interacting physics. The MSR concept is one such example, where the neutronics and thermal-hydraulics are tightly coupled through the Doppler effect and the temperature dependence of liquid fuel salt density.

MOOSE, and Moltres by extension, are capable of up to 3-D geometry modelling. They support a wide range of input mesh file formats listed in a MOOSE webpage, including the commonly used Exodus II file format. Specifically for the 2-D case, axial symmetry is easily and automatically imposed by changing one line of code in the input file, without any changes in the Cartesian representations of the PDEs and boundary conditions in their original C++ implementations. This feature provides significant computational time savings for 3-D systems that exhibit high axial symmetry. Another important feature for reducing computational time is the use of MPI for parallel computing. All MOOSE-based codes can be compiled and run on high performance computing clusters.

MOOSE includes a set of built-in physics modules for commonly studied phenomena such as the heat conduction, flow dynamics and solid mechanics. This work uses MOOSE's Navier-Stokes module for simulating incompressible salt flow in the MSFR. Peterson et al. verified the incompressible flow capabilities in the Navier-Stokes module and presented results for common CFD problems such as the lid-driven cavity, axisymmetric channel, and flow-over-a-sphere problems [50].

### 3.3 Moltres

Moltres is an application built in the MOOSE parallel finite element framework [11]. Similar to the physics modules in MOOSE, Moltres contains the necessary kernels representing various physics and boundary conditions for solving for the neutron flux, delayed neutron precursor concentration, and temperature. Together with the Navier-Stokes module, it solves the deterministic multigroup neutron diffusion and thermal-hydraulics PDEs simultaneously on the same mesh. Moltres supports up to 3-D meshes and scales well over a large number of processors. The underlying MOOSE framework provides a range of implicit and explicit methods for the coupling between the neutronics and thermal-hydraulics governing equations.

In the introductory journal article for Moltres, Lindsay et al. [11] demonstrated Moltres' capabilities with 2D-axisymmetric and 3D models of the MSRE. The results showed good qualitative agreement with legacy MSRE data with some minor quantitative discrepancies due to a number of differences in the legacy model. Since then, Moltres has undergone further development in the past three years. The authors of the first paper have since developed various new capabilities in Moltres, most significantly providing support for looping delayed neutron precursors back into the core, and a pointwise heat removal kernel to simulate a heat exchanger. The present author demonstrated these capabilities in a 2-D axisymmetric model of the MSFR with uniform salt flow [51].

Building on the prior progress, this thesis presents two more recent developments in Moltres, namely the new kernels required to couple incompressible flow with the delayed neutron precursor looping capability, and introducing a decay heat model to simulate decay heat from fission products. The incompressible flow profile from MOOSE's Navier-Stokes module provides a more accurate representation of the flow profile, precursor movement, and heat transfer as opposed to assuming uniform velocity fields featured in the previous papers [11, 51].

### 3.4 Modeling Approach

This section discusses the neutronics and thermal-hydraulics PDEs that Moltres solves and other relevant details specific to the MSFR model in this work.

As mentioned in the previous chapter, the fuel salt loop is divided into two regions, the central

core region where most of the fissions take place, and the outer loop region where the heat exchanger is located. The central core region specifically refers to the central region indicated by the red box in Figure 3.1. The outer loop is simplified into a 1-D pipe as it is a subcritical region and its main purposes are: to introduce an out-of-core residence time for the DNPs, and to contain the heat removal kernel to simulate the heat exchanger. Accordingly, this section provides separate descriptions for the governing equations in the central core region and the outer loop region. There is also a third region comprised of the blanket salt, the NiCrW Hastelloy reflectors, and other material. This region is important for capturing a more accurate estimate of neutron leakage than would imposing fixed albedo neutron flux boundary conditions.

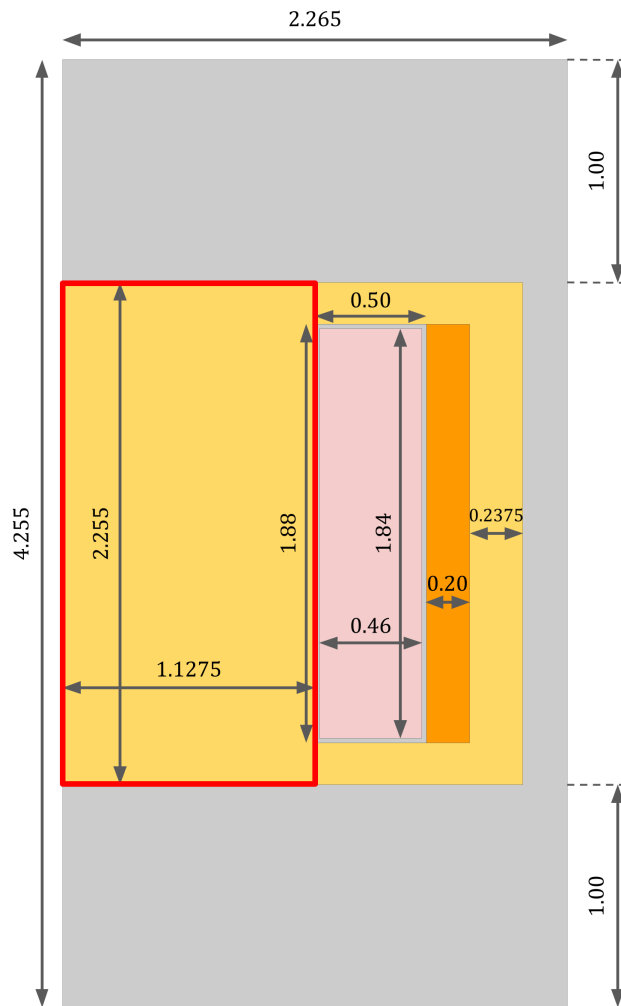


Figure 3.1: 2-D axisymmetric model of the MSFR. The red box indicates the central core region in the modeling approach in Moltres.

### 3.4.1 Central Core Region

The central core region is of greatest interest to us during steady state and transient scenarios; the center of the reactor is naturally where most of the fissions and heat generation occur.

#### Neutronics Model

The neutron flux calculations in the central core region are performed using the standard formulations for the time-dependent multigroup neutron diffusion equations and DNP concentration equations as shown in equations 3.1 and 3.2:

$$\frac{1}{v_g} \frac{\partial \phi_g}{\partial t} = \nabla \cdot D_g \nabla \phi_g - \Sigma_g^r \phi_g + \sum_{g' \neq g}^G \Sigma_{g' \rightarrow g}^s \phi_{g'} + \chi_g^p \sum_{g'=1}^G (1 - \beta) \nu \Sigma_{g'}^f \phi_{g'} + \chi_g^d \sum_i^I \lambda_i C_i, \quad (3.1)$$

$$\frac{\partial C_i}{\partial t} = \beta_i \sum_{g'=1}^G \nu \Sigma_{g'}^f \phi_{g'} - \lambda_i C_i - \vec{u} \cdot \nabla C_i + \nabla \cdot K \nabla C_i, \quad (3.2)$$

where

$v_g$  = average speed of neutrons in group  $g$  [ $\text{cm} \cdot \text{s}^{-1}$ ],

$\phi_g$  = neutron flux in group  $g$  [ $\text{cm}^{-2} \cdot \text{s}^{-1}$ ],

$t$  = time [s],

$D_g$  = diffusion coefficient of neutrons in group  $g$  [ $\text{cm}^2 \cdot \text{s}^{-1}$ ],

$\Sigma_g^r$  = macroscopic cross section for removal of neutrons from group  $g$  [ $\text{cm}^{-1}$ ],

$\Sigma_{g' \rightarrow g}^s$  = macroscopic cross section of scattering from  $g'$  to  $g$  [ $\text{cm}^{-1}$ ],

$\chi_g^p$  = prompt fission spectrum for neutrons in group  $g$ ,

$G$  = total number of discrete neutron groups,

$\nu$  = average number of neutrons produced per fission,

$\Sigma_g^f$  = macroscopic fission cross section for neutron in group  $g$  [ $\text{cm}^{-1}$ ],

$\chi_g^d$  = delayed fission spectrum for neutrons in group  $g$ ,

$I$  = total number of delayed neutron precursor groups,

$\beta$  = total delayed neutron fraction,

$\beta_i$  = delayed neutron fraction of precursor group  $i$ ,

$\lambda_i$  = average decay constant of delayed neutron precursors in precursor group  $i$  [ $\text{s}^{-1}$ ],

$C_i$  = concentration of delayed neutron precursors in precursor group  $i$  [ $\text{cm}^{-3}$ ],

$K$  = turbulent diffusion of the delayed neutron precursors [ $\text{cm}^2 \cdot \text{s}^{-1}$ ].

While the limitations of the multigroup neutron diffusion compared to other deterministic and Monte Carlo methods, particularly for flux values near boundaries, are well-documented, the diffusion model provides acceptable accuracy at lower computational costs. Moreover, the central core region contains no material interfaces except at its boundaries. Chapter 4 provides a comparison of the MSFR multiplication factor values and reactivity coefficients between Moltres and Serpent.

The DNP concentration equation has additional advection and turbulent diffusion terms to account for the movement of DNPs in the primary coolant loop. The turbulent diffusion  $K$  is governed by the following equation:

$$K = \frac{\mu_t}{\rho S_{c_t}} \quad (3.3)$$

where

$\mu_t$  = eddy viscosity [ $\text{Pa s}$ ],

$\rho$  = density of the fuel salt [ $\text{kg m}^{-3}$ ],

$S_{c_t}$  = turbulent Schmidt number.

This work assumes  $S_{c_t} = 0.85$  for a fair comparison with the Polimi and TUDelft models [9] which used the same value. It has its roots in the Reynolds Analogy which states that turbulent momentum and heat transfer largely depend on the same eddies in turbulent flow [52]. Therefore,  $S_{c_t}$  should be close to unity.  $S_{c_t} = 0.85$  is also the default value for most commercial CFD software [52].

Moltres users may vary the total number of neutron energy groups as long as they provide Moltres with the appropriate group constant data. The number of precursor groups is also variable, though usually predetermined by the choice of nuclear data library in the group constant generation



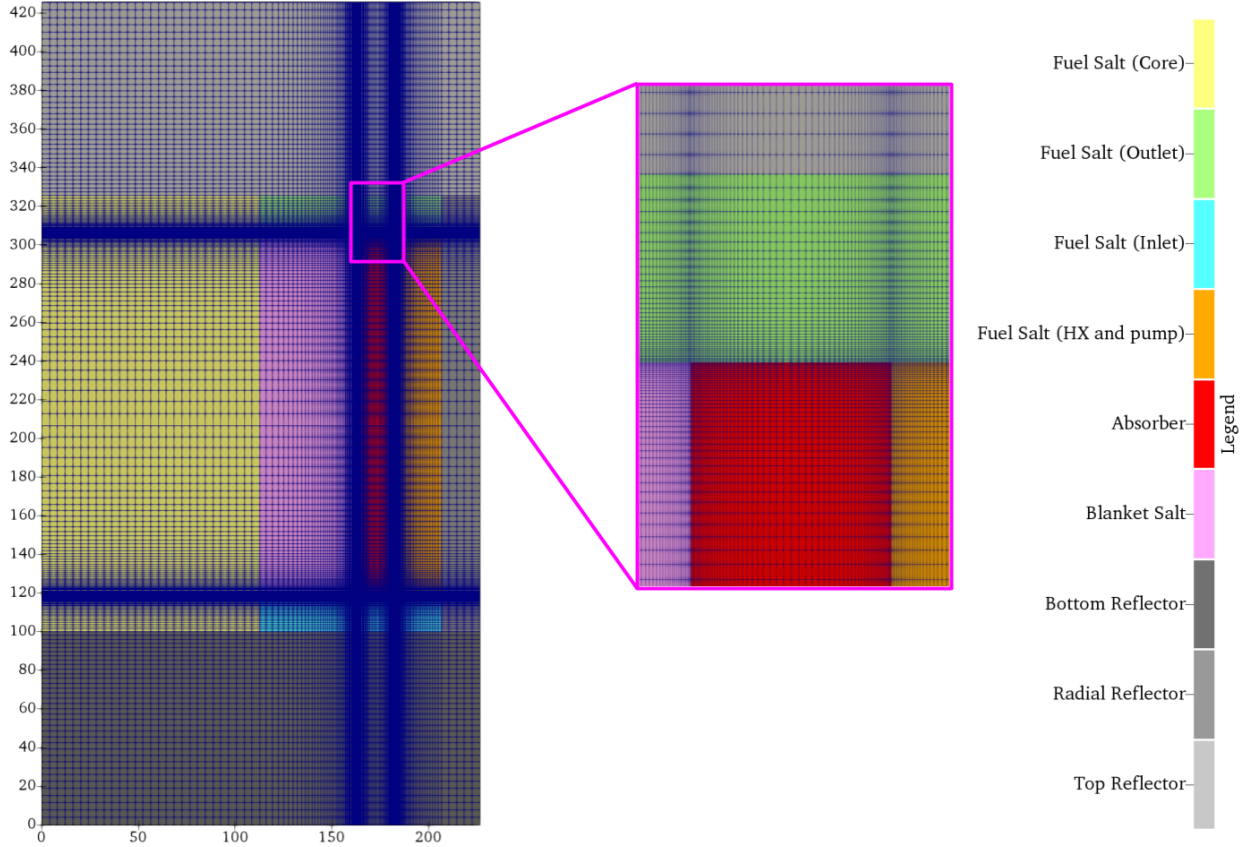


Figure 3.2: Mesh adopted in Moltres and a close-up view of the mesh around the boron carbide absorber.

step. Moltres automatically interpolates the group constant data for required temperatures using one of the many predefined interpolation methods available in MOOSE. Once again, Moltres allows users to select their interpolation method of choice.

The MSFR model in this work uses six neutron energy groups according to the energy boundaries in table 3.1, and eight DNP groups as defined by the JEFF-3.1.2 library. The neutron flux and DNP concentration values were approximated by first-order Lagrange and constant monomial shape functions respectively on the finite element mesh. Figure 3.2 shows the mesh adopted for the MSFR model. This work assumes vacuum boundary conditions for all six neutron group fluxes along the external boundaries of the geometry, and homogeneous Neumann boundary conditions along the axial symmetry boundary. For the DNP concentrations, we imposed homogeneous Neumann boundary conditions on the walls, and inflow and outflow boundary conditions on the inlet and outlet boundaries respectively. The inlet DNP concentration values were imported from the outlet

values of the 1-D outer loop pipe at the same timestep.

For the decay heat model, a previous study on the MSFR by Aufiero et al. [53] showed that using three decay heat precursor groups with appropriate half-lives in the form of exponential equations, can accurately model decay heat in the MSFR for up to 300 seconds after shutdown with a relative error of less than 2%. Thus, this thesis implements the new decay heat modeling capability with the following equation:

$$\frac{\partial \omega_j}{\partial t} = f_j \sum_{g=1}^G \epsilon_g \Sigma_g^f \phi_g - \lambda_j \omega_j - \vec{u} \cdot \nabla \omega_j + \nabla \cdot K \nabla \omega_j, \quad (3.4)$$

where

$\omega_j$  = total decay heat power density from decay heat precursors in group  $j$  [ $\text{W} \cdot \text{cm}^{-3}$ ],

$f_j$  = fraction of decay heat from group  $j$  to total power under full-power conditions,

$\epsilon_g$  = average fission energy per fission [W],

$\lambda_j$  = average decay constant of decay heat precursors in group  $j$  [ $\text{s}^{-1}$ ].

Like the neutron and DNP groups, Moltres can accommodate an arbitrary number of decay heat groups. This work uses the same decay heat fractions and decay constants, shown in Table 3.4, used in the Polimi and TUDelft models for three decay heat groups.

Table 3.2: Decay heat group parameters [9].

Decay heat group $j$	$\lambda_j$ [ $\text{s}^{-1}$ ]	$f_j$
1	0.1974	0.0117
2	0.0168	0.0129
3	0.000 358	0.0186

## Thermal-Hydraulics Model

This work models fluid dynamics using the incompressible Navier-Stokes (INS) capabilities from the MOOSE Navier-Stokes module [50]. The standard INS equations are:

$$\text{Momentum eq.:} \quad \rho \frac{\partial \vec{u}}{\partial t} = -\rho(\vec{u} \cdot \nabla)\vec{u} + \nabla \cdot (-p\vec{I} + \mu[\nabla\vec{u} + (\nabla\vec{u})^T]) + \vec{f} \quad (3.5)$$

$$\text{Divergence-free:} \quad \nabla \cdot \vec{u} = 0 \quad (3.6)$$

where

$$p = \text{pressure [Pa]},$$

$$\mu = \text{dynamic viscosity [Pa s]},$$

$$\vec{f} = \text{body force per unit volume [N}\cdot\text{m}^{-3}\text{]}.$$

In addition to the intrinsic molecular viscosity, this thesis introduces an eddy viscosity term to approximate turbulent flow effects. The current implementation of the Navier-Stokes module does not have a turbulence model such as the RANS models used in the Polimi and TUDelft models [9]. Thus, this work uses a zeroth-order approximation of the eddy viscosity based on the results reported in the Polimi/TUDelft models. The eddy viscosity is assumed to be 40 Pa s. Despite the simplicity of this assumption, the resulting flow profile is similar to flow profile in the Polimi and TUDelft models at steady state.

The energy balance equation for temperature used in this Moltres model is:

$$\rho c_p \frac{\partial T}{\partial t} = -\rho c_p \vec{u} \cdot \nabla T + \nabla \cdot [(k + k_t)\nabla T] + Q_s \quad (3.7)$$

$$k_t = \frac{\mu_t}{\rho Pr_t} \quad (3.8)$$

$$Q_s = \left(1 - \sum_{j=1}^J f_j\right) \sum_{g=1}^G \epsilon_g \Sigma_g^f \phi_g + \sum_{j=1}^J \omega_j, \quad (3.9)$$

where

$c_p$  = specific heat capacity of molten salt [ $\text{J}\cdot\text{kg}^{-1}\cdot\text{K}^{-1}$ ],

$T$  = temperature of molten salt [K]

$\vec{u}$  = velocity of molten salt [ $\text{m}\cdot\text{s}^{-1}$ ],

$k$  = thermal conductivity of molten salt [ $\text{W}\cdot\text{m}^{-1}\cdot\text{K}^{-1}$ ],

$J$  = total number of decay heat groups.

The diffusion term includes turbulent heat diffusivity based on the eddy viscosity  $\mu_t$  and the turbulent Prandtl number  $Pr_t$ .  $Pr_t$  is also 0.85 due to the same reasoning provided for  $Sc_t$ . The first term in the heat source  $Q_s$  equation represents prompt fission heat, and the second term represents decay heat from the  $J$  decay heat groups.

With this model, the results were expected to show good qualitative agreement with the Polimi and TUDelft models, including the large recirculation region near the blanket tank walls and the resulting high temperatures in that region. The results in Chapter 5 would be some minor discrepancies where the viscosity values are under- or over-predicted, leading to minor inaccuracies in temperature and precursor concentration distributions from turbulent diffusion.

## Boundary Conditions

Table 3.3 summarizes the boundary conditions for all variables on all of the relevant boundaries. Figure 3.3 shows the locations of the various boundaries listed in the table.

Table 3.3: Boundary conditions in the main reactor geometry (Figure 3.3).

Variable	Boundary	Boundary Condition
Neutron flux $\phi_g$	Top	$\left. \frac{d\phi_g}{dx} \right _{\text{inflow}} = 0$
	Outer	$\left. \frac{d\phi_g}{dx} \right _{\text{inflow}} = 0$
	Bottom	$\left. \frac{d\phi_g}{dx} \right _{\text{inflow}} = 0$
	Axial	$\frac{d\phi_g}{dx} = 0$
Delayed neutron precursor concentration $C_i$	Top (Core)	$\frac{dC_i}{dx} = 0$
	Bottom (Core)	$\frac{dC_i}{dx} = 0$
	Outer (Core)	$\frac{dC_i}{dx} = 0$
	Axial (Core)	$\frac{dC_i}{dx} = 0$
	Inlet (Core)	$C_i = c$
	Outlet (Core)	$u_x \cdot C_i = 0$
Decay heat power density $\omega_j$	Top (Core)	$\frac{d\omega_j}{dx} = 0$
	Bottom (Core)	$\frac{d\omega_j}{dx} = 0$
	Outer (Core)	$\frac{d\omega_j}{dx} = 0$
	Axial (Core)	$\frac{d\omega_j}{dx} = 0$
	Inlet (Core)	$\omega_j = c$
	Outlet (Core)	$u_x \cdot \omega_j = 0$
Radial velocity $u_x$	Top (Core)	$u_x = 0$
	Bottom (Core)	$u_x = 0$
	Outer (Core)	$u_x = 0$
	Axial (Core)	$u_x = 0$
	Inlet (Core)	$u_x = c$
	Outlet (Core)	$\frac{du_x}{dx} = 0$
Axial velocity $u_y$	Top (Core)	$u_y = 0$
	Bottom (Core)	$u_y = 0$
	Outer (Core)	$u_y = 0$
	Axial (Core)	$\frac{du_y}{dx} = 0$
	Inlet (Core)	$u_y = 0$
	Outlet (Core)	$\frac{du_y}{dx} = 0$
Temperature $T$	Top (Core)	$\frac{dT}{dx} = 0$
	Bottom (Core)	$\frac{dT}{dx} = 0$
	Outer (Core)	$\frac{dT}{dx} = 0$
	Axial (Core)	$\frac{dT}{dx} = 0$
	Inlet (Core)	$T = c$
	Outlet (Core)	$\frac{dT}{dx} = 0$

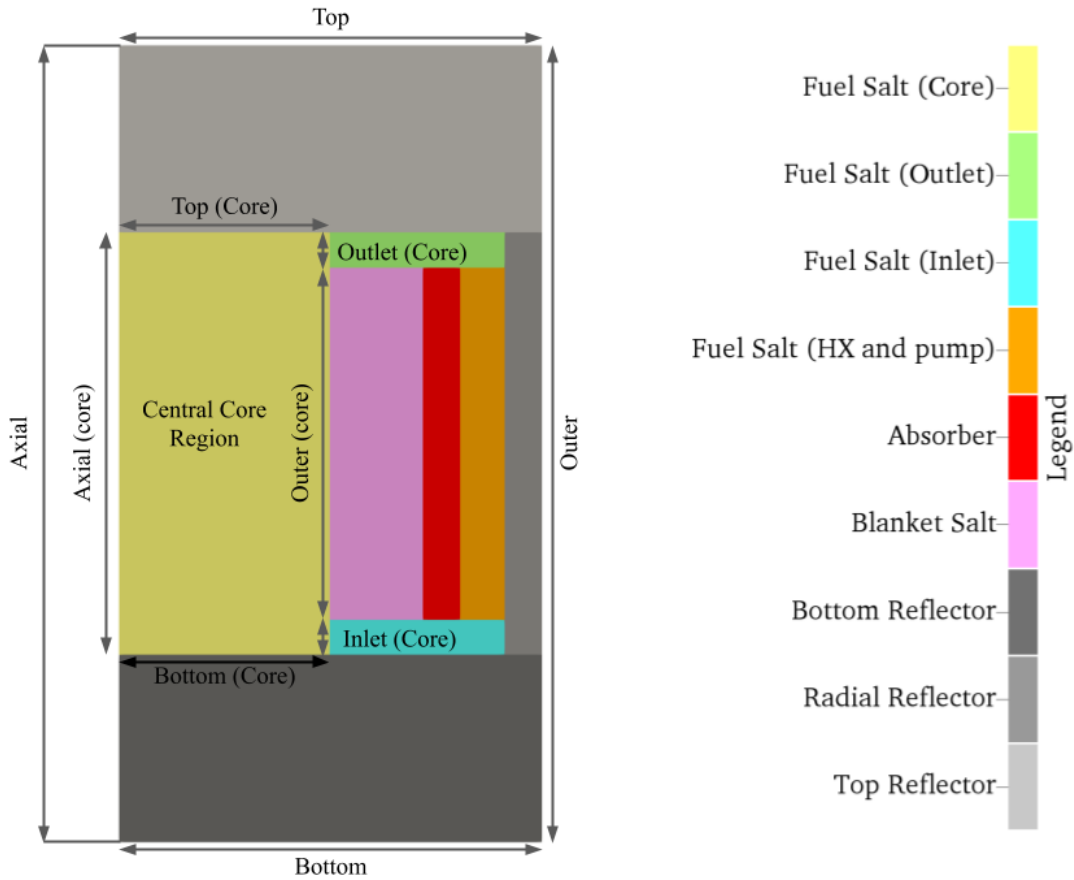


Figure 3.3: The boundaries in the MSFR geometry that are relevant for the boundary conditions mentioned in Table 3.3.

### 3.4.2 Outer Loop Region

Moltres also accounts for the decay of DNPs outside the central core region by simulating its flow in a separate 1-D pipe geometry. This outer loop pipe simulation is implicitly coupled to the active core simulation through Picard iterations in MOOSE’s MultiApp functionality and inlet/outlet boundary values. For this work with the MSFR model, we assumed a pipe length of 2.255 m with salt flowing at  $1.1275 \text{ m s}^{-1}$  for an average out-of-core residence time of 2 seconds to follow the design specifications.

## Neutronics Model

Since this outer loop region is largely subcritical, the only significant neutronics-related phenomena are the drift and decay of DNPs. The governing equation for the DNPs is:

$$\frac{\partial C_i}{\partial t} = -\lambda_i C_i - u \frac{\partial C_i}{\partial x}. \quad (3.10)$$

Equation 3.10 is derived from equation 3.2 by removing the fission DNP source term, and the conversion of the advection and diffusion terms to their 1-D forms. The decay constants and diffusion coefficient are the same values used in the central core region.

## Thermal-Hydraulics Model

A constant velocity of  $1.1275 \text{ m s}^{-1}$  is applied in the outer loop region. The governing equation for temperature, derived from equation 3.7, is:

$$\rho c_p \frac{\partial T}{\partial t} = -\rho c_p u \frac{\partial T}{\partial x} - Q_{hx} \quad (3.11)$$

$$Q_{hx} = \alpha(T - T_i)\delta(x_0) \quad (3.12)$$

where

$Q_{hx}$  = heat removal rate through the heat exchanger [W],

$\alpha$  = heat transfer coefficient [ $\text{W}\cdot\text{K}^{-1}$ ],

$T_i$  = temperature of the intermediate salt [K],

$x_0$  = position of the point heat exchanger [m].

The fission heat source term is replaced with a heat exchanger sink term  $Q_{hx}$  which depends on the temperature difference between the fuel salt  $T$  and the intermediate loop salt  $T_i$ . For simplicity, this work assumes a constant temperature of 823 K in the intermediate loop. The heat transfer coefficient was determined by assuming that the fuel outlet temperature is 1023 K and calculating the heat removal rate to induce a 100 K drop at the given volumetric flow rate and heat capacity of

the fuel salt. The resulting value for  $\alpha$  is  $370.668 \text{ W}\cdot\text{K}^{-1}$ . This work opted to ignore the diffusion term due to the discontinuity of the temperature distribution across the point heat exchanger.

## Boundary Conditions

Table 3.4 summarizes the boundary conditions for all variables on the inlet and outlet of the 1-D outer loop region.

Table 3.4: Boundary conditions in the 1-D outer loop geometry.  $u$  represents the 1-D velocity in this region.

Variable	Boundary	Boundary Condition
Delayed neutron precursor concentration $C_i$	Inlet (Core)	$C_i = c$
	Outlet (Core)	$u \cdot C_i = 0$
Decay heat power density $\omega_j$	Inlet (Core)	$\omega_j = c$
	Outlet (Core)	$u \cdot \omega_j = 0$
Temperature $T$	Inlet (Core)	$T = c$
	Outlet (Core)	$u \cdot T = 0$

### 3.4.3 Flow Transfers

This subsection details the delayed neutron and decay heat precursors, and temperature flow transfers between the central core and outer loop regions.

A parabolic flow profile was imposed on the inlet Dirichlet boundary condition. The equation for  $u_x$  at the inlet is:

$$u_x = -2034.01 \left[ \frac{y}{18.75} - \left( \frac{y}{18.75} \right)^2 \right] \quad (3.13)$$

where

$$y = \text{height along the inlet [cm]}. \quad (3.14)$$

The inlet is 18.75 cm high, and the coefficient at the front is from normalizing the equation for a total volumetric flow rate of  $4.5 \text{ m}^3 \text{ s}^{-1}$ .

At every timestep, Moltres also calculates weighted averages of the temperature and the



precursors at the outlet. These values are weighted by the outflow velocity values at the outlet according to the following equation:

$$\bar{\psi} = \frac{\int_{\mathcal{C}} \psi(y)u(y)dy}{\int_{\mathcal{C}} u(y)dy} \quad (3.15)$$

where

$\psi$  = variable to be weighted

$\mathcal{C}$  = outlet boundary curve

$u$  = outflow velocity perpendicular to the outlet boundary [ $\text{m s}^{-1}$ ].

This outflow value from the central core region is transferred to the 1-D outer loop region as input for the inhomogeneous Dirichlet boundary condition at the inlet boundary. Likewise, the outflow value from the outer loop region is used for the inflow value in the central core region. No averaging is required for this step as the outer loop region is a 1-D system. We assume that the inflow temperature and DNP are uniform at the inlet. The Picard iterations within every timestep ensure that the two systems are implicitly coupled even though they're solved separately.

# Chapter 4

## Neutronics Results

This chapter compares key neutronics results between Serpent and Moltres for a static model of the MSFR, i.e. no salt flow, and uniform temperature distribution to assess the accuracy of the six-group neutron diffusion model in Moltres on a fast-spectrum reactor. This verification exercise builds on a previous study by Lindsay et al. [11] that had verified Moltres' neutronics capabilities with a two-group neutron diffusion model of the MSRE.

### Details of the static MSFR model on Moltres

- No salt flow (static salt)
- Uniform temperature of 973 K throughout the 2D core model
- Six neutron energy groups
- Eight delayed neutron precursor groups
- Vacuum boundary conditions on the outer boundaries of the 2D core mesh

### 4.1 Effective Multiplication Factor and Delayed Neutron Fraction

Moltres solves the six-group neutron diffusion equations as a steady-state eigenvalue problem to find the  $k_{\text{eff}}$  for the static MSFR model. Table 4.1 shows the  $k_{\text{eff}}$  values from Serpent 2 and Moltres at 973 K and the corresponding salt density, and Table 4.2 shows the  $k_{\text{eff}}$  values for other temperatures at 100 K intervals. We observe small discrepancies on the order of 100 pcm between the two codes which we attribute to two main factors: the accuracy of the neutron diffusion model, and the omission of the blanket tank structural material in Moltres. The neutron diffusion model is

not as accurate as the other  $S_N$  or  $SP_N$  deterministic methods nor the Monte Carlo approach in Serpent. Regarding the omission of the blanket tank material, we replaced the 2 cm-thick structural material with blanket salt. This replacement may be partly responsible for the higher  $k_{\text{eff}}$  value calculated by Moltres as the macroscopic fission cross sections of the blanket salt are non-zero for the higher neutron energy groups. Nevertheless, the discrepancy is smaller than the 228.5 pcm and 256.7 pcm discrepancies reported by Cervi et al. [54] for their six-group  $SP_3$  and neutron diffusion methods, respectively, in OpenFOAM. Aufiero et al. [10] used the same neutron diffusion model in OpenFOAM for their transient analysis of the MSFR, albeit with one neutron energy group to reduce computational load.

Table 4.1:  $k_{\text{eff}}$  values from Serpent 2 and Moltres at 973 K.

Code	$k_{\text{eff}}$
Serpent 2	1.006 62(5)
Moltres with DNPs	1.007 940 0(10)
Moltres without DNPs	1.004 919 7(10)

Table 4.2:  $k_{\text{eff}}$  values from Serpent 2 and Moltres at various temperatures from 800 K to 1400 K.

Temperature [K]	$k_{\text{eff}} \pm \sigma$ (Serpent 2)	$k_{\text{eff}}$ (Moltres)	Difference wrt Serpent 2 [pcm]
800	1.019 96(5)	1.021 17	121
900	1.011 72(5)	1.013 22	150
1000	1.004 28(5)	1.005 44	116
1100	0.997 35(5)	0.998 59	124
1200	0.990 06(5)	0.991 19	113
1300	0.983 56(5)	0.984 39	83
1400	0.977 02(5)	0.978 20	118

The absolute value of  $k_{\text{eff}}$  impacts the final steady-state temperature of the reactor. We can raise or lower the average core temperature at steady state to meet the design specifications for the inlet and outlet temperatures by adjusting the fissile inventory and  $k_{\text{eff}}$ . In transient analysis, the delayed neutron fraction  $\beta$  and reactivity coefficients  $\alpha$  are important as they dictate the duration, shape, and magnitude of the reactor transient response. The difference between  $\beta$  and  $\beta_{\text{eff}}$  is that  $\beta$  is the physical delayed neutron fraction while  $\beta_{\text{eff}}$  is the delayed neutron fraction weighted on the adjoint neutron flux. We will compare the  $\beta$  value from Moltres to the  $\beta_{\text{eff}}$  value from Serpent because Moltres currently lacks a adjoint calculation capability. We calculated  $\beta$  by taking the relative difference between the  $k_{\text{eff}}$  values with and without DNPs in Table 4.1. The  $\beta$  and  $\beta_{\text{eff}}$

values at 973 K, shown in Table 4.3, are in good agreement with a 4.43 pcm discrepancy.

Table 4.3:  $\beta_{\text{eff}}$  and  $\beta$  values from Serpent 2 and Moltres, respectively, at 973 K.

Code	$\beta_{\text{eff}}$ [pcm]	Difference wrt Serpent [pcm]
Serpent	304.08(81)	-
Moltres	299.65(20)	4.43

## 4.2 Reactivity Feedback Coefficients

The temperature reactivity feedback arises mainly from Doppler broadening of resonance absorption peaks and temperature-induced density changes. Although Doppler coefficients typically show logarithmic dependence to temperature, we report them, along with the other coefficients, as linear gradient values of the reactivity given the relatively linear trend within the relevant temperature range (Figure 4.1). The temperature range extends below the melting point of the fuel salt (873 K) to ensure that the data covers the relevant range between 873 K and 900 K. Table 4.4 shows the temperature coefficients as described prior. The total temperature coefficients from Serpent and Moltres show excellent agreement with a discrepancy of 0.019 pcm K<sup>-1</sup>.

Table 4.4: Doppler, density, and total temperature coefficients for the temperature range of 800 K to 1400 K.

Software	$\alpha_D$ (log) [pcm]	$\alpha_D$ (linear) [pcm K <sup>-1</sup> ]	$\alpha_\rho$ [pcm K <sup>-1</sup> ]	$\alpha_T$ [pcm K <sup>-1</sup> ]
Serpent	-4034(14)	-3.737(13)	-3.424(13)	-7.165(13)
Moltres	-	-	-	-7.184

## 4.3 Neutron Energy Spectrum

Moltres also closely replicated the six-group neutron spectrum from the Serpent group constants. Figure 4.2 compares the neutron energy spectra from Serpent and Moltres in the central fuel salt region. The six-group neutron spectra overlap exactly over each other. More generally, the plot shows the distinctive fast spectrum observed in the MSFR with dips in the spectrum corresponding to elastic scattering resonances from lithium and fluorine. From this plot, we observe that the discrepancies in  $k_{\text{eff}}$  arise mainly from discretizing neutron energy into groups rather than the

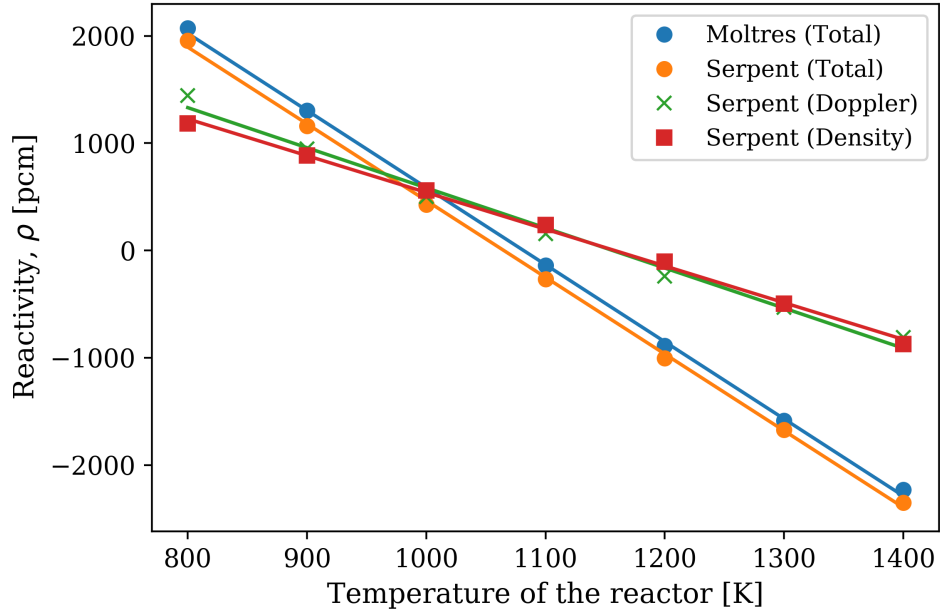


Figure 4.1: Reactivity values from Serpent and Moltres. The Doppler reactivity values were calculated at a fixed density of  $4.1249 \text{ g cm}^{-3}$ . The density reactivity values were calculated at a fixed temperature of 973 K.

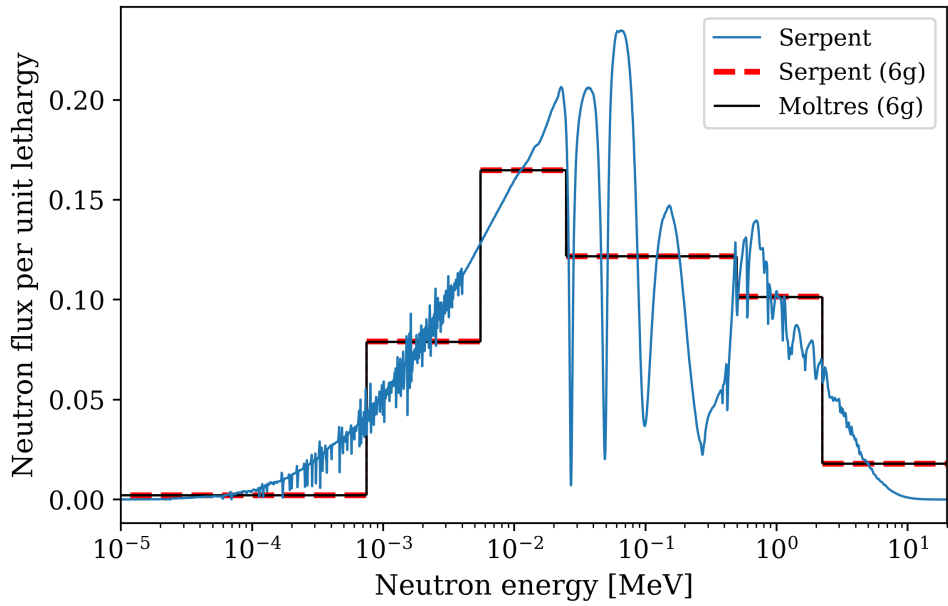


Figure 4.2: The fine-group and six-group neutron energy spectra from Serpent 2 and Moltres normalized per unit lethargy.

neutron diffusion model itself. We could obtain a more accurate representation of the neutronics in the MSFR by using more neutron energy groups but this would adversely impact simulation times in the subsequent multiphysics finite element analyses.

In summary, Moltres replicated most of the relevant neutronics parameters accurately with the group constant data from Serpent. Moltres agrees with the high fidelity simulation in Serpent 2 for the  $\beta_{\text{eff}}$  and temperature reactivity coefficients, which are important parameters for modeling transient reactor behavior. The  $k_{\text{eff}}$  values have discrepancies on the order of 100 pcm and they are relatively small compared to the  $k_{\text{eff}}$  values from the neutron diffusion and SP3 models in OpenFOAM [54].

## Chapter 5

# Coupled Neutronics/Thermal-Hydraulics Steady-State Results

With the verification of Moltres' neutronics modeling capabilities in the context of the MSFR, this chapter will cover the steady-state multiphysics simulation results from Moltres.

The procedure for obtaining the steady-state results involved several steps due to the tightly coupled PDEs. First, a preliminary transient simulation of fluid flow in the MSFR core was run, starting from zero inlet velocity and gradually ramping up to match the nominal flow rate ( $4.5 \text{ m}^3 \text{ s}^{-1}$ ); otherwise Moltres had difficulty converging to the desired fully developed flow profile. Next, these fully developed flow values were imported as initial values for velocity in the full time-dependent simulation modeling the full coupled neutronics and thermal-hydraulics multiphysics model. The initial values for the temperature and neutron group flux distributions are 953 K and  $1 \times 10^{14} \text{ cm}^{-2} \text{ s}^{-1}$  uniformly throughout the geometry. Finally, this work assumes that steady state is reached when the volume integral values of every variable remain constant (up to 6 sig. fig.) for at least four seconds in the simulation; this time period corresponds to the nominal circulation time of the MSFR.

For a direct comparison with the steady-state results from the Polimi and TUDelft models [10], this chapter will first present the steady-state results without modeling decay heat. After this comparison, the chapter separately discusses the minor differences in the results from decay heat modeling in the last subsection.

### 5.1 Steady-State Thermal-Hydraulics Results

Figure 5.1 shows the temperature and velocity fields of the fuel salt in the core at steady state from Moltres and the Polimi and TUDelft models. Figure 5.2 provides an alternate view of the flow profile through flow streamlines superimposed on the velocity magnitude distribution. The

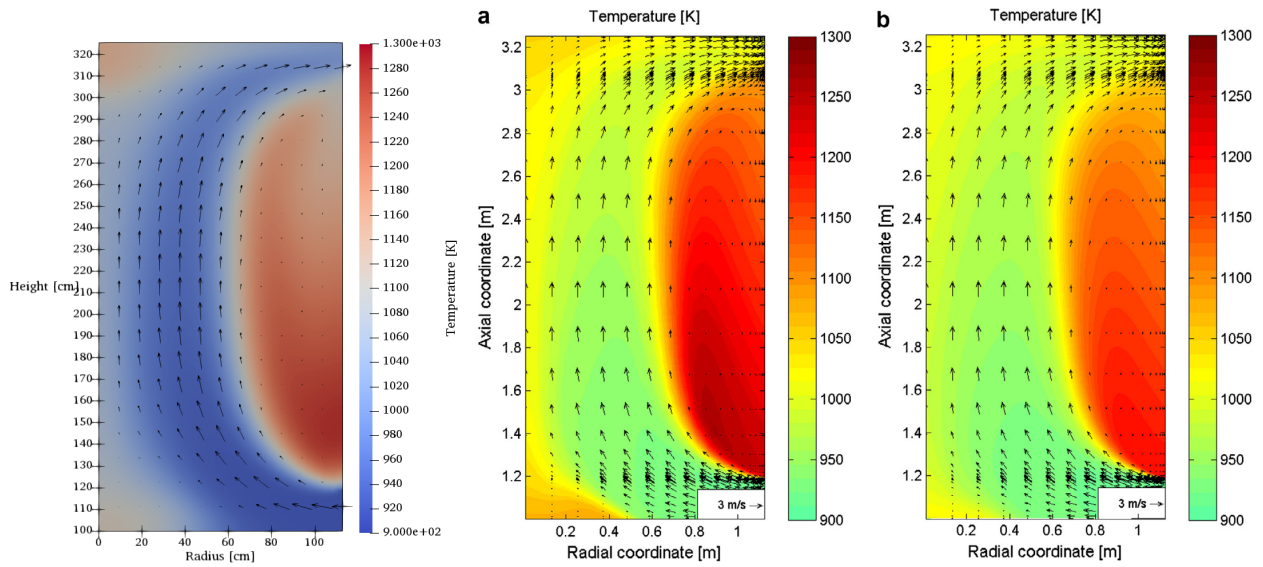


Figure 5.1: Temperature and velocity fields in the core from Moltres (left), Polimi (center), and TUDelft (right) models. The colors represent temperature according to the respective colorbars and the arrows represent velocity fields.

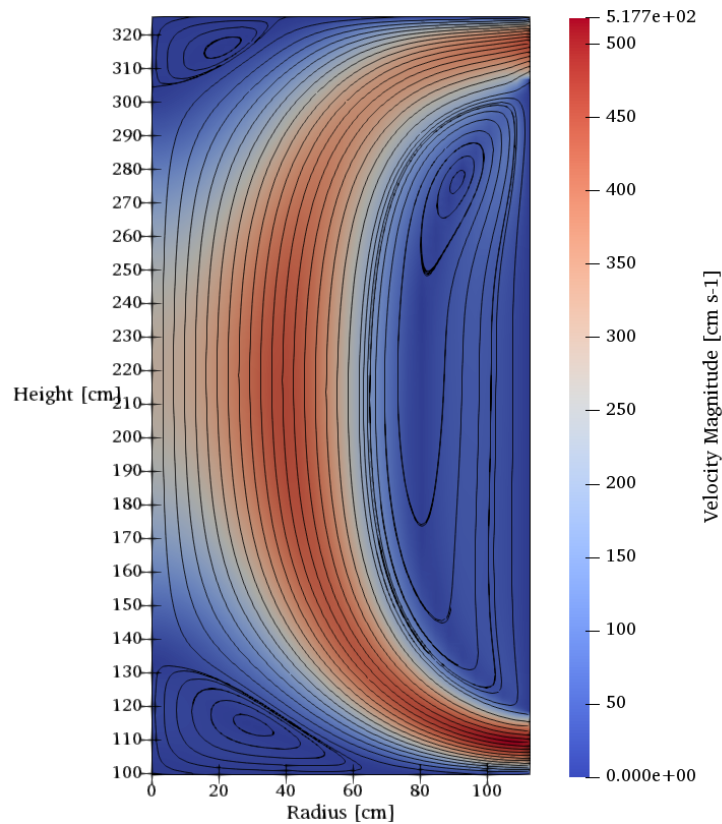


Figure 5.2: Fuel salt flow streamlines and velocity magnitude in the core. The colors represent velocity magnitude according to the colorbar on the right.



results from Moltres show good qualitative agreement with the Polimi and TUDelft models [9]; the plots show similar flow and hotspot features in all three models. Furthermore, the highest salt velocities in all three models occur at the inlet, outlet, and at core half-height approximately 0.40 m away from the central axis. A large recirculation region forms near the blanket tank walls from turbulent flow. Inertial forces dominate over viscous forces to form this large eddy. The main difference between Moltres and Fiorina et al.'s models is the flow profile near the central axis at the top and bottom of the core. The Polimi and TUDelft models predict relatively stagnant flow in these regions without recirculation. Moltres, on the other hand, predicts explicit recirculating flow in these regions. This is due to our constant turbulent viscosity approximation in Moltres. The  $k-\epsilon$  turbulence models in the Polimi and TUDelft models predict that the turbulent viscosity in these regions is as high as 100 Pa s, much higher than our 40 Pa s approximation.

Nevertheless, similar temperature hotspots form in these regions of recirculation and stagnation as convection is the dominant heat transfer mechanism. The maximum temperature from Moltres, 1275 K near the bottom of the large recirculation zone, is closer to the maximum temperature in the Polimi model ( $\approx 1300$  K) than the TUDelft model ( $\approx 1200$  K). Similarly, the plots show cooler temperatures in high-velocity regions. The minimum temperature is 924 K at the inlet.

Although the temperatures at the hotspots are well below the melting point of the Ni-alloy structure (1500 K), they may cause undue thermal stress on the blanket tank structure and induce relatively faster salt corrosion rates. A sudden, large reactivity insertion could push fuel salt temperatures above the melting point of the Ni-alloy and cause irreversible damage. Furthermore, the reservoir of hot fuel salt may cause unpredictable behavior during transient scenarios when the flow profile undergoes a drastic change. Thus, Rouch et al. [55] developed an improved hourglass-shaped design to optimize flow distribution and prevent these recirculation zones and hotspots from forming. A study of this new design using Moltres is a potential subject for future work when a proper turbulence model is in place.

## 5.2 Steady-State Neutronics Results

### 5.2.1 Neutron Flux

The neutron flux distribution represents the heat source distribution in a nuclear reactor. Figure 5.3 shows the neutron flux distributions in the core for all six neutron energy groups, and Figure 5.4 shows the axial and radial fluxes along the center of the core and at reactor half-height, respectively. The distributions are highly symmetric along the central and horizontal axes, as expected of a cylindrical reactor design. The relatively lower temperatures near the center of the core promotes the neutron flux peaking but it is of little concern as no structural parts vulnerable to neutron damage exist in that region. The peak total flux at the center is  $9.80 \times 10^{15} \text{ cm}^{-2}\cdot\text{s}^{-1}$ , which is close to values reported by Fiorina et al. [56] and Aufiero et al. [10] as shown in Table 5.1. The peak flux value from this paper is slightly higher as this work used the steady-state temperature distribution while Fiorina et al. and Aufiero et al. imposed a uniform temperature distribution at 973 K.

### 5.2.2 Delayed Neutron Fraction

As mentioned earlier, the delayed neutron precursors (DNPs) are mobile in MSRs and their distributions do not directly correspond to the neutron flux distributions. The location where the DNPs decay and emit neutrons impacts their neutron importance depending on their proximity to fissile and parasitic isotopes. Figure 5.5 shows the DNP distributions for all eight DNP groups. In general, the figures show less DNPs in the regions with fast salt flow. The precursors from the shortest-lived group (Group 8) predominantly decay within the core as their half-lives are shorter than the time it takes to reach the outlet while the precursors from the longest-lived group (Group 1) are relatively evenly distributed due to their long half-lives. For the longer-lived groups, the DNP concentrations are ill-resolved on the mesh elements adjacent to the outlet and the inlet

Table 5.1: Peak neutron flux values from Moltres (this paper), COMSOL [56], and OpenFOAM [10] models along with the temperature distribution with which the values were obtained.

Model	Temperature distribution	Peak Neutron Flux [ $\times 10^{15} \text{ cm}^{-2} \text{ s}^{-1}$ ]
Moltres (This paper)	Steady state	9.80
COMSOL	Uniform, 973 K	8.6
OpenFOAM	Uniform, 973 K	9.0

boundaries, respectively. Thus, the present author recommends careful mesh refinement for future work involving similar geometries.

Figure 5.6 compares the total delayed neutron source distribution from Moltres with the results from the Polimi and TUDelft models [9]. In contrast to Figure 5.5 which shows the precursor distribution, Figure 5.6 shows the rate of delayed neutron emission, which was calculated by multiplying each DNP group  $C_i$  with its associated decay constant  $\lambda_i$ . The Polimi and TUDelft models feature greater DNP retention in the stagnant regions within the core. This effect is less pronounced in the Moltres model. Less build-up of DNPs at the top of the core occurs in Moltres because most of the DNPs produced near the center of the core cannot enter the axial recirculation

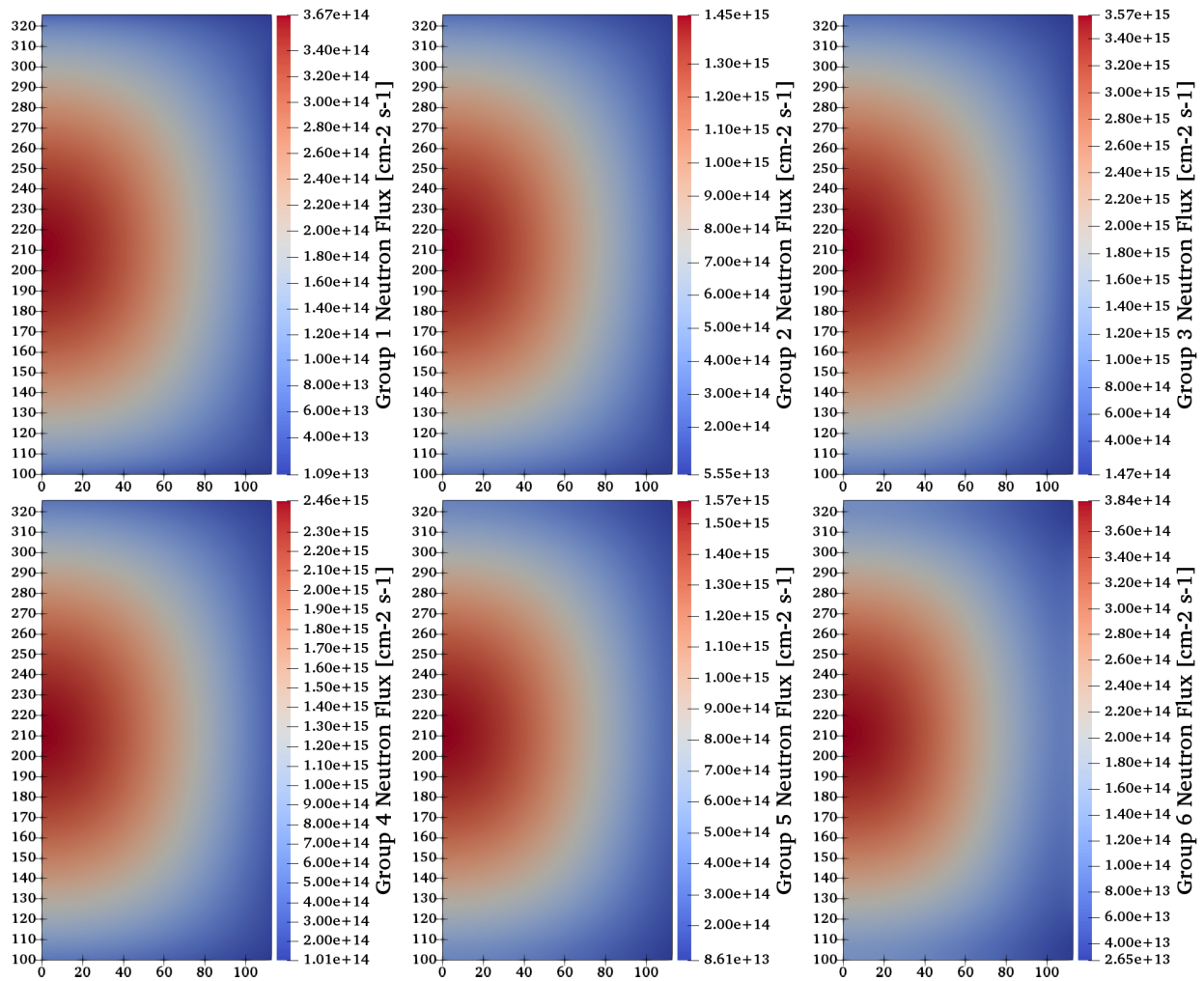


Figure 5.3: Neutron flux distributions in the core for neutron energy groups 1 to 6. The y and x axes represent height and radius (in cm) of the core relative to the entire reactor geometry.

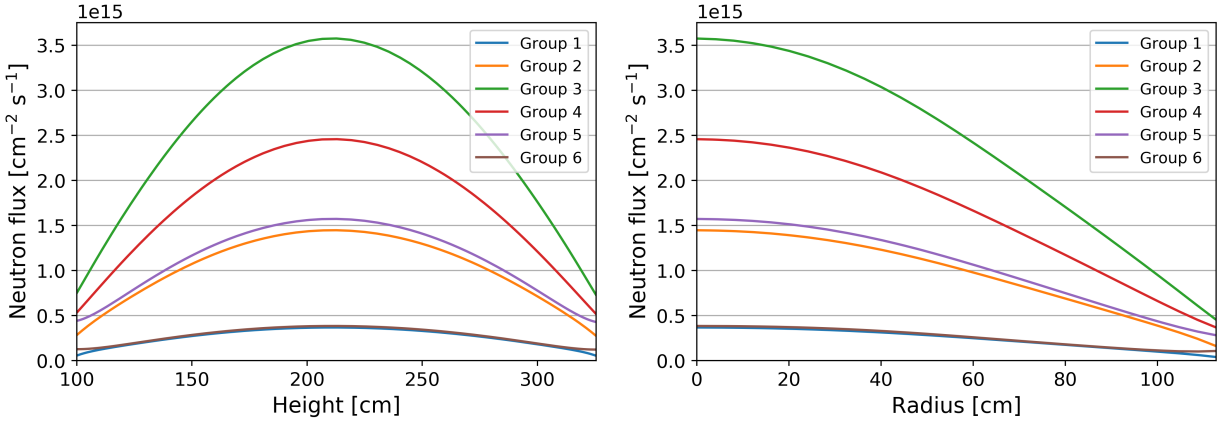


Figure 5.4: Axial (left) and radial (right) neutron flux distributions in the core for neutron energy groups 1 to 6.

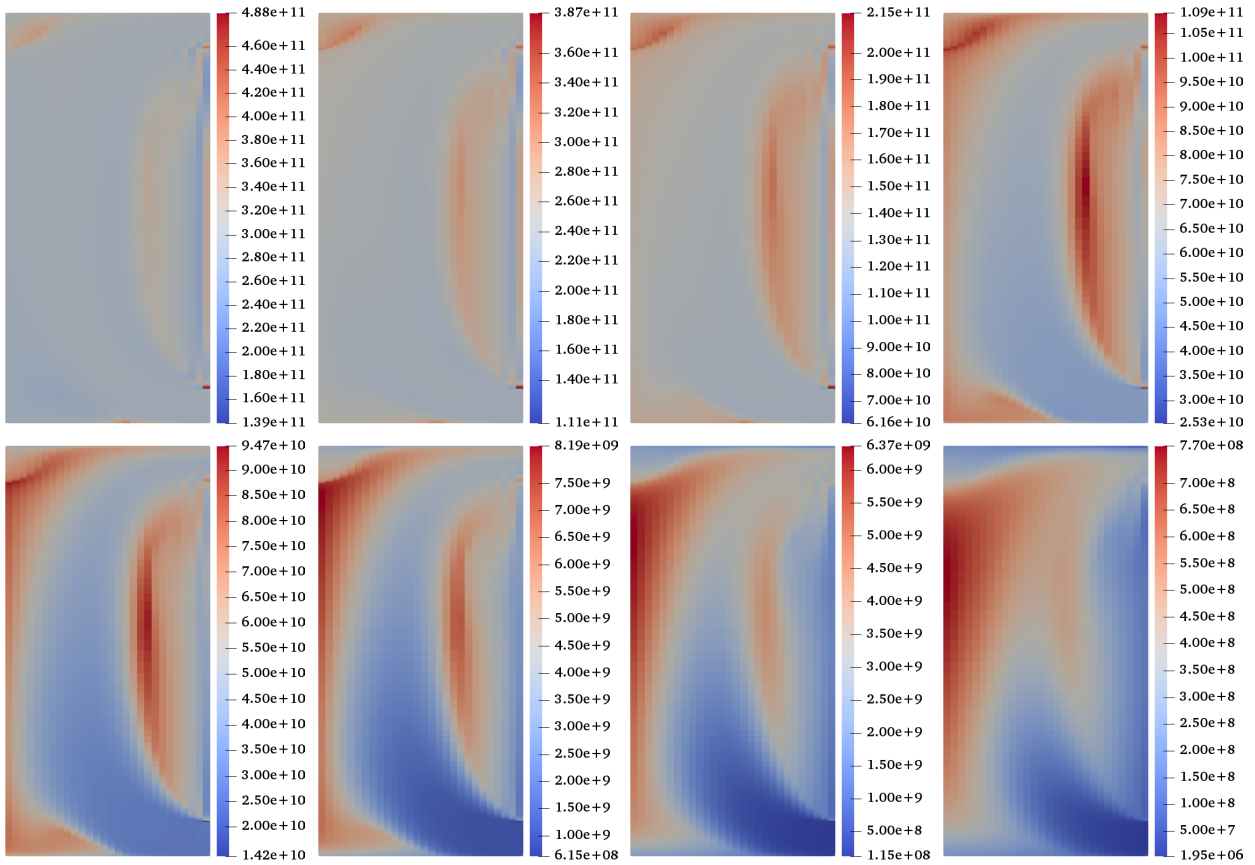


Figure 5.5: DNP distributions in the core for DNP groups 1 to 8 (from left to right, top to bottom). Refer to Figure 5.3 for the height and radius scales on the y and x axes, respectively. Note the different scales for each distribution.

zone that only appears in Moltres. The figure also shows less build-up in the large recirculation zone near the blanket tank.

The in-core delayed neutron fraction  $\beta_c$  is an important safety parameter for MSRs. This value represents the actual delayed neutron fraction in MSRs after accounting for the loss of delayed neutrons from DNPs decaying outside the active core region. Reactors with smaller  $\beta$  values exhibit greater prompt jumps in the neutron flux in response to reactivity insertions because they have a greater proportion of prompt neutrons under normal operating conditions. This is undesirable from a reactor safety perspective because it exposes the reactor to relatively more extreme conditions before active safety mechanisms activate and scram the reactor. In MSRs, this danger is partly mitigated by the strong, negative fuel temperature reactivity coefficient. Chapter 6 contains more in-depth discussions for various transient scenarios.

Table 5.2 compares the fraction of out-of-core emissions and the  $\beta_c$  values from Moltres with the Polimi and TUDelft models. We calculated the fraction of out-of-core emissions by finding the total amount of each DNP group in the core and the outer loop, multiplying each total by their associated decay time constants  $\lambda_i$ , and calculating the proportion of emissions in the outer loop relative to the grand total. We calculated  $\beta_c$  by first obtaining the prompt neutron emission rate from Moltres and subsequently using in-core delayed neutron emission rate from the previous calculation to find the fraction of delayed neutron emission rate relative to total emission rate.

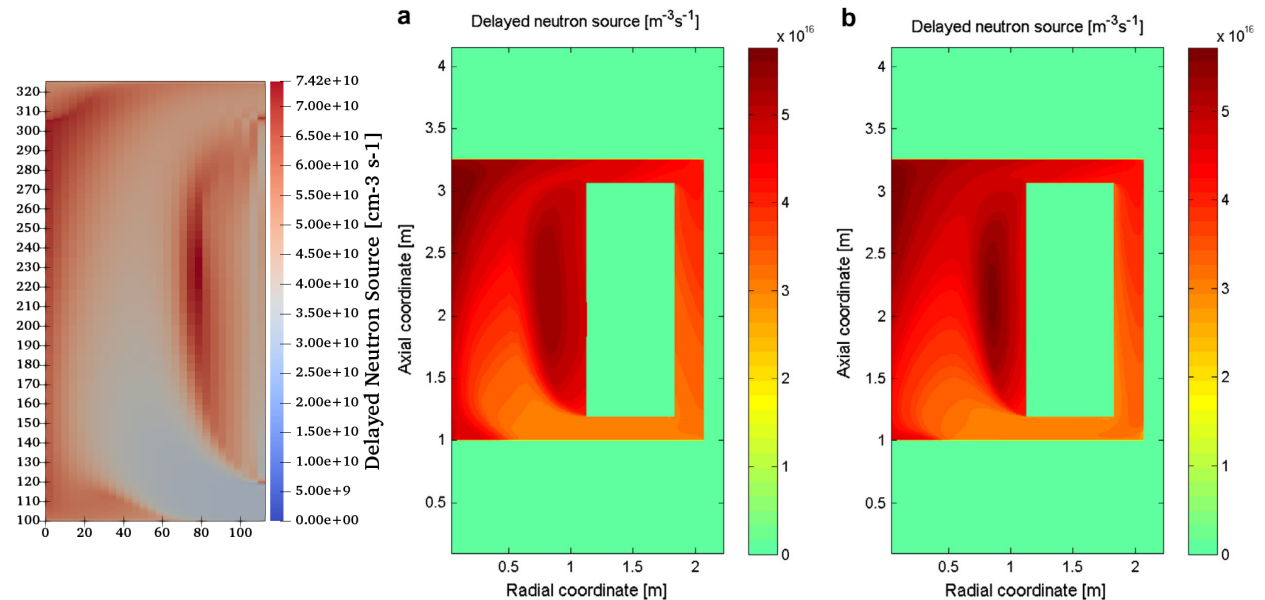


Figure 5.6: Total delayed neutron source distribution in the core from Moltres (left), Polimi (center), and TUDelft (right) models.

Table 5.2: The fraction of delayed neutrons lost from out-of-core emission and the in-core delayed neutron fraction  $\beta_c$  values from Moltres (this paper), and the Polimi and TUDelft models [9].

Model	Out-of-Core Emission [%]	$\beta_c$ [pcm]
Moltres (This paper)	44.16	184.9
Polimi	34.80	134.3
TUDelft	34.85	123.8

The fraction of out-of-core emissions from our Moltres model differs significantly by approximately 10%, and  $\beta_c$  differs by 60-70 pcm. The former is attributed to the lesser DNP retention in the stagnant flow regions in the core; the DNPs are more evenly distributed along the entire primary loop, leading to more delayed neutron emissions in the outer loop region. This is likely caused by differences in the flow pattern in the recirculation zone because convective transport dominates diffusive effects in the MSFR. The exact flow pattern in the recirculation zones in the Polimi and TUDelft models is likely to differ from that in Moltres (Figure 5.2). Figure 5.1 also shows some minor differences in the magnitude of the flow in the recirculation zones between Moltres, and the Polimi and TUDelft models. Although the sizes of the arrows representing flow velocity are on different scales, a quick comparison between the largest arrows and the arrows in the recirculation zone indicates that the recirculation zone in Moltres is relatively more stagnant. This could explain the concentration of DNPs along an “arc” closer to the center of the core in Moltres as opposed to the more even distribution of DNPs throughout the whole recirculation zones in the Polimi and TUDelft models. The higher peak DNPs distribution in Moltres also supports this assertion.

In spite of the greater delayed neutron losses, the  $\beta_c$  value is higher in Moltres than the Polimi and TUDelft models. To account for this peculiarity, Fiorina et al. [9] applied adjoint flux weighting for their  $\beta_c$  calculation whereas this work reports the value as the physical fraction without adjoint weighting. The weighting results in a significant difference in  $\beta_c$  because a greater fraction of the DNPs decay in the recirculation zones, where the neutron importance is noticeably diminished.

### 5.3 Decay Heat

The inclusion of a decay heat model effectively redistributes a fraction of the volumetric heat source from the center of the core to the entire loop. Thus, there should be a slight flattening of the

temperature distribution across the entire primary loop.

## Chapter 6

# Transient Scenarios

This chapter discusses the transient multiphysics simulation results of the MSFR from Moltres for four accident scenarios. These scenarios, adapted from Fiorina et al.'s work [9], include unprotected instances of reactivity insertion, loss of heat sink, loss of flow, and pump overspeed accidents. The term “unprotected” means no external interventions occur in these scenarios. As such, these simulations give an insight on the MSFR's passive safety capabilities in the absence of any active safety system. This work used the steady-state configuration presented in the previous chapter as the initial conditions for the transient simulations discussed in this chapter. Specifically, all steady-state spatial values for neutron flux, delayed neutron precursor concentration, temperature, velocity, and pressure were imported as the initial state of the transient scenarios.

As noted by Fiorina et al. [9], explicit decay heat modeling has a negligible effect in reactivity-, and pump-initiated transients. Furthermore, only their Polimi model had decay heat modeling capabilities. Therefore, they presented results from their Polimi and TUDelft model for the four accident scenarios without decay heat modeling and enabled decay heat modeling for the loss of heat sink transient scenario only. This work also ran all transient simulations without the decay heat model for a fair comparison. The only exception is loss of heat sink scenario in which two separate simulations with and without the decay heat model were run. More generally, this work imposed various other simplifying assumptions in our transient models to match their implementations as closely as possible, within Moltres' capabilities. The details of the setup for each transient simulation are in their respective sections.



## 6.1 Unprotected Reactivity Insertion

Reactivity insertion accidents are a type of nuclear accident caused by unintended positive reactivity insertions. The excess reactivity causes the power output and temperatures in nuclear reactors to rise to potentially dangerous levels. In MSRs, a positive reactivity insertion could occur when the online refueling system injects excess fissile material into the core. Excessively high neutron fluences and temperatures negatively impact reactor structural integrity and increase the risk of containment breach.

This work modeled two unprotected step-wise reactivity insertion scenarios in Moltres by swapping out the original set of group constant data with two new, separate sets of data from Serpent corresponding to 50 pcm and 200 pcm reactivity insertions, respectively. The reactivity of the Serpent MSFR models was increased by increasing the  $^{233}\text{U}$ -to- $^{232}\text{Th}$  ratio in the fuel salt.

The focus of this transient study is the neutronic and thermal-hydraulic behavior of the reactor core. Thus, this work assumes that the heat exchanger and the associated power generation equipment (generator turbines, heat sinks, etc.) can withstand all variations in the power output during the transients.

Figures 6.1 and 6.2 show the power output and average core temperature increase following the 50 pcm step-wise reactivity insertion in the Moltres, Polimi, and TUDelft models. The initial prompt response to the reactivity insertion raises power to 4 GW by  $t = 0.001$  s. Figure 6.3 shows the rise in power output specifically during the prompt response in a separate plot. Power continues to rise at a slower rate up to 4.63 GW at around  $t = 0.005$  s, at which point the negative reactivity from the Doppler effect and salt expansion becomes greater than the initial +50 pcm insertion. Power continues to fall as the average core temperature rises. The slight change in slope occurs at  $t = 0.3$  s. The elapsed time approximately corresponds to the average half-life of the two shortest-lived delayed neutron precursor (DNP) groups ( $t_{1/2} = 0.195$  s and 0.424 s); the decay of the surplus precursors produced in the initial phase negates a fraction of the negative reactivity from the elevated core temperature. By  $t = 3$ -4 s, most of the heated salt and DNPs from the initial phase will have circulated around the primary loop and returned to the core. The heated salt causes a small, noticeable dip in power before the power output stabilises. The core tends to a new equilibrium average temperature approximately 7.5 K higher than the initial average temperature.

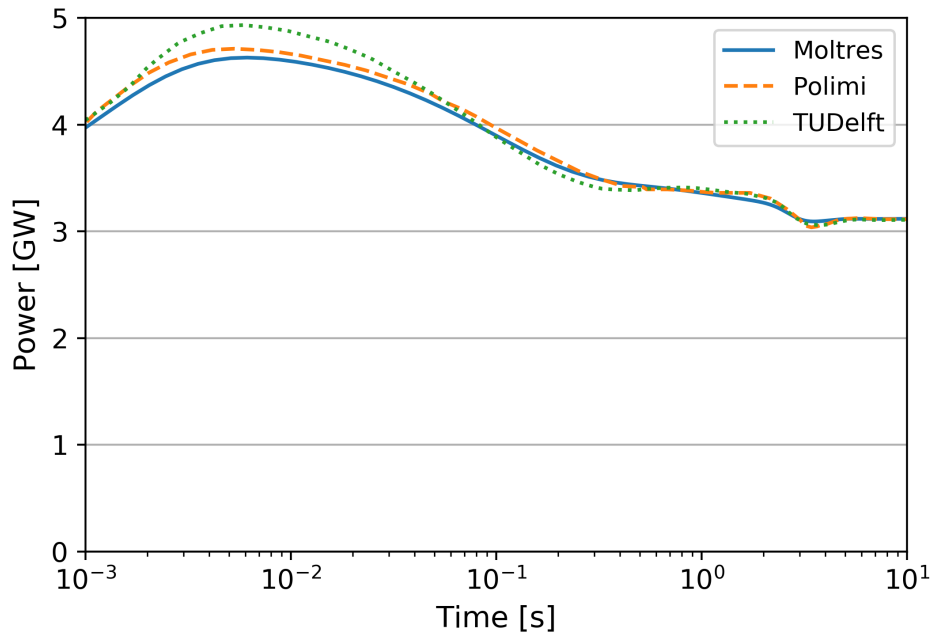


Figure 6.1: Power output following a 50 pcm step-wise reactivity insertion in the Moltres, Polimi, and TUDelft models [9].

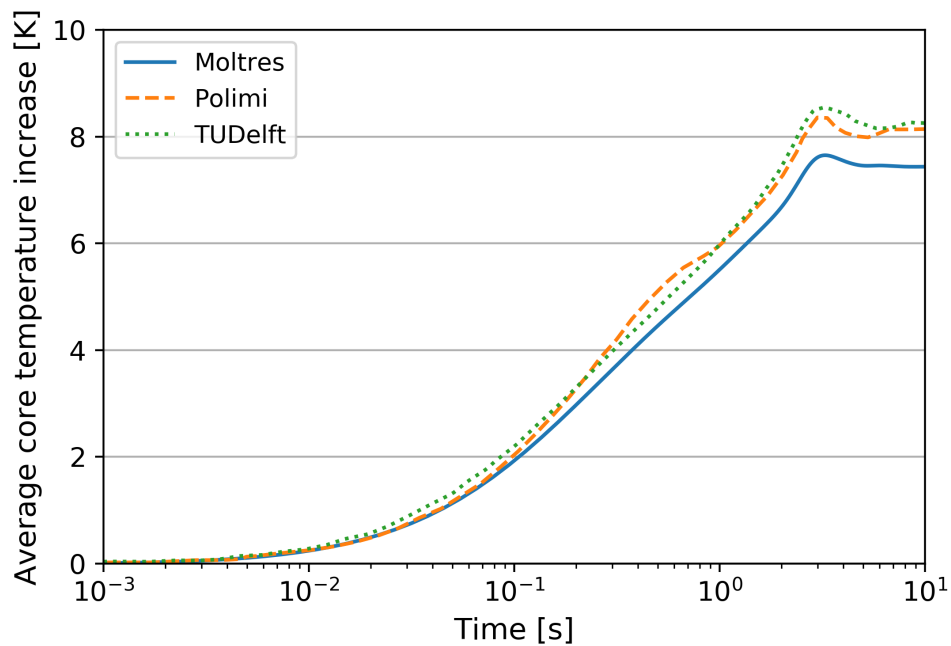


Figure 6.2: Average core temperature increase following a 50 pcm step-wise reactivity insertion in the Moltres, Polimi, and TUDelft models [9].

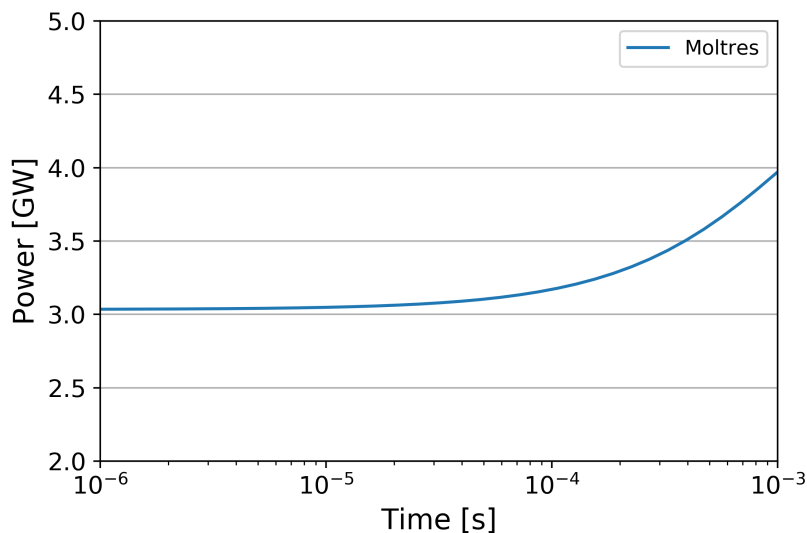


Figure 6.3: Power output during the prompt response following a 50 pcm step-wise reactivity insertion in the Moltres, Polimi, and TUDelft models [9].

The results from Moltres show good agreement with the results from the Polimi and TUDelft models; Moltres reproduced all of the individual features in both plots. The magnitude of the reactor response is the most significant difference. Moltres predicts a smaller peak in the power output and a smaller overall increase in the average core temperature mainly due to the more negative temperature reactivity coefficient in Moltres than in the Polimi and TUDelft models. The temperature reactivity coefficient  $\alpha_T$  in Moltres is  $-7.184$  pcm  $K^{-1}$  (Table 4.4), as opposed to approximately  $-6.5$  pcm  $K^{-1}$  within the relevant temperature range in the Polimi and TUDelft models. Therefore, the results show a smaller temperature increase in the Moltres model for the same reactivity insertion. Multiplying the average core temperature increase at  $t = 10$  s with  $\alpha_T$  gives us  $-7.184$  pcm  $K^{-1} \times 7.46$  K =  $-53.6$  pcm, which is approximately equal to the 50 pcm reactivity insertion.

The results for the 200 pcm reactivity insertion scenario show similar trends to the 50 pcm case. The greater reactivity insertion elicits a stronger prompt response in the power output which peaks at 92.1 GW. The average core temperature increases much more rapidly and subsequently triggers a sharper drop in power output. This results in the clearer distinction in the rate of core temperature increase before and after  $t = 0.01$  s. In this transient, we also observe greater deviation between Moltres and the other models arising from the differences in the temperature reactivity coefficients.

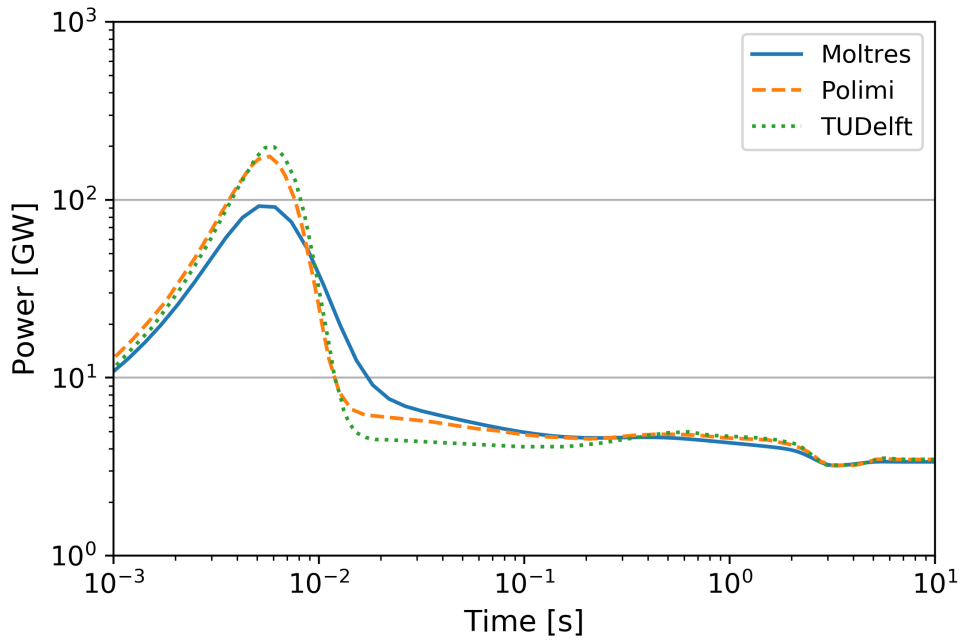


Figure 6.4: Power output following a 200 pcm step-wise reactivity insertion in the Moltres, Polimi, and TUDelft models [9].

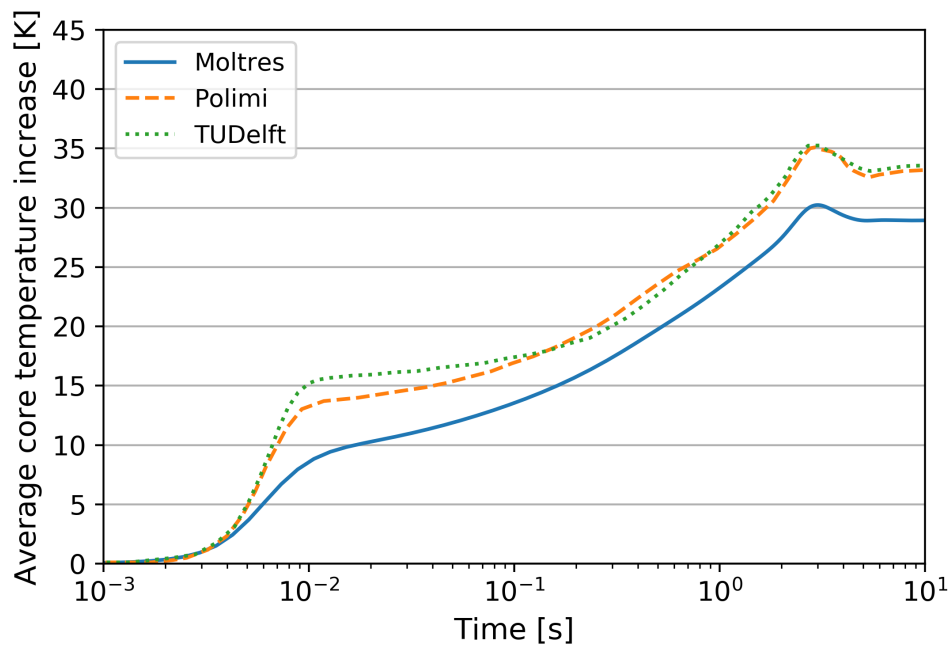


Figure 6.5: Average core temperature increase following a 200 pcm step-wise reactivity insertion in the Moltres, Polimi, and TUDelft models [9].

Overall, Moltres' results show good agreement with the Polimi and TUDelft results. The differences arise mainly due to the differences in the temperature reactivity coefficients.

## 6.2 Unprotected Loss of Heat Sink

An unprotected loss of heat sink accident can occur when the pumps in the intermediate loop fail. The heat exchangers would then lose most of their cooling capabilities. This work followed Fiorina et al.'s approach in assuming that the cooling from the heat exchangers decreases exponentially with a time constant of 1 s and all other parameters held constant [9]. As mentioned in the Chapter 5, we will present two sets of results for this transient: 1) without decay heat modeling, and 2) with decay heat modeling.

### 6.2.1 Without Decay Heat

Figures 6.6 and 6.7 show the power output and average core temperature increase during the unprotected loss of heat sink transient in the Moltres, Polimi, and TUDelft models without decay heat modeling. The power output and average core temperature show little change in the first two seconds as it takes approximately that amount of time for the partially cooled salt to migrate to the center of the core. At  $t = 2$  s, we observe a sharp spike in average core temperature and a corresponding drop in power output. The presence of delayed neutron precursors (DNPs) from the steady-state operating conditions momentarily halt the increase in temperature at around  $t = 5$  s. The average core temperature continues to rise while the power output falls through the rest of the transient.

The results from Moltres show good agreement with the results from the Polimi and TUDelft. Moltres reproduced all of the trends in the Polimi and TUDelft models. The temporary halt in the temperature increase occurs at a lower average core temperature for Moltres than the other two models. This is likely due to the difference in the temperature reactivity coefficient discussed in the reactivity insertion results; a smaller increase in the average core temperature produces the same decrease in power output.

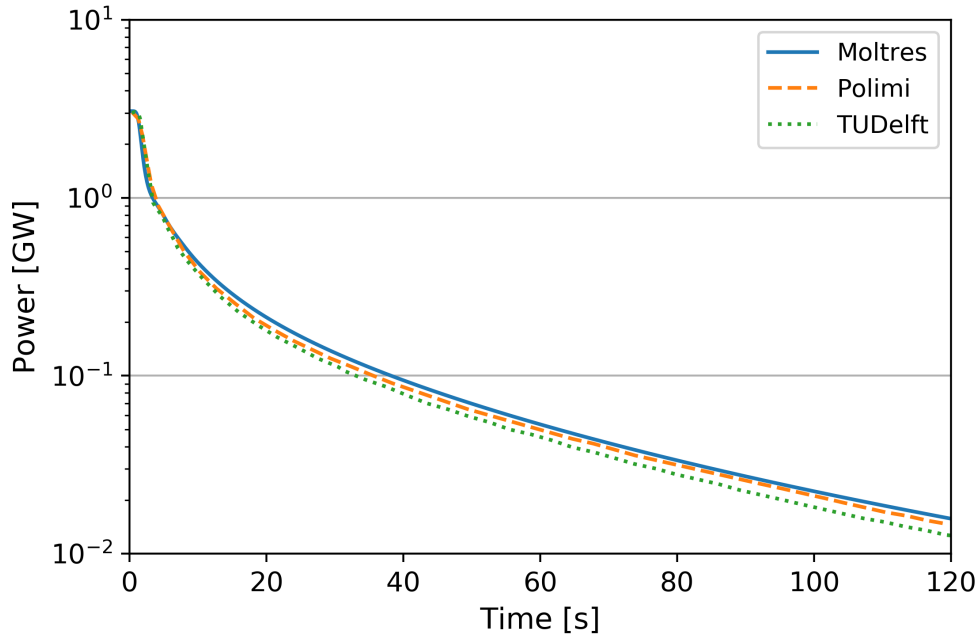


Figure 6.6: Power output during an unprotected loss of heat sink transient in the Moltres, Polimi, and TUDelft models [9] without decay heat.

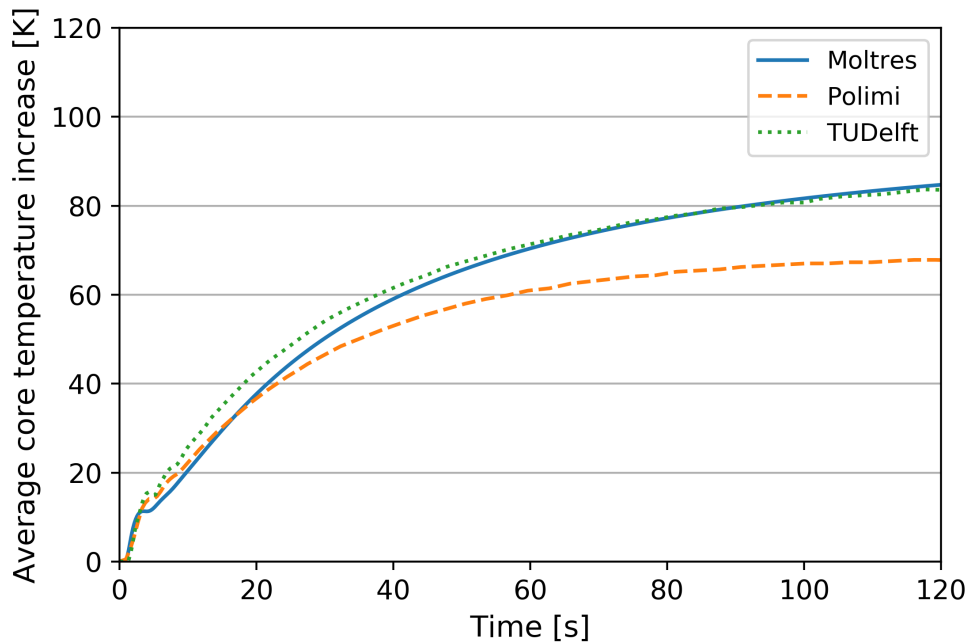


Figure 6.7: Average core temperature increase during an unprotected loss of heat sink transient in the Moltres, Polimi, and TUDelft models [9] without decay heat.

## 6.2.2 With Decay Heat



### 6.3 Unprotected Loss of Flow

A loss of forced flow transient can occur in the event of a station blackout; the pumps would cease operating due to the loss of AC electrical power. Natural circulation resulting from temperature-dependent density changes becomes the dominant driving force for salt flow in the primary loop. Fiorina et al. [9] applied the Boussinesq approximation for buoyancy-driven flow in their models, but this approach was not possible in Moltres because the primary loop is partitioned into two separate geometries and used Dirichlet boundary conditions at the inlet to drive flow. Fiorina et al.'s Polimi and TUDelft models featured complete exponential coast-downs of the pumps with a time constant of 5 s. The resulting flow rate  $\dot{m}$  from natural circulation was approximately 18 times smaller than the initial  $\dot{m}$ . Figure 6.8 shows that the actual  $\dot{m}$  decreased with a time constant of 8 s. Thus, for the MSFR model in Moltres, this work imposed a similar exponential decay term with a time constant of 8 s on the inflow Dirichlet boundary condition:

$$\text{Flow rate, } v = 0.25862 + (4.5 - 0.25862)e^{-t/8} \quad (6.1)$$

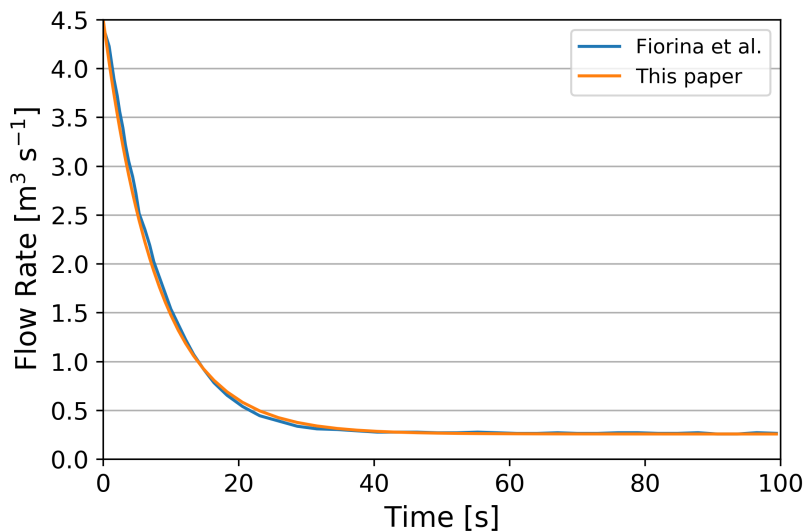


Figure 6.8: The change in flow rate in the Polimi and TUDelft models and the imposed flow rate in Moltres.

The reduced  $\dot{m}$  also decreases the heat transfer rate between the primary and intermediate loop through the heat exchanger as the heat transfer coefficient  $h$  is dependent on the  $\dot{m}$ . This step was

problematic because the pointwise heat exchanger implementation in Moltres performs differently compared with the heat exchangers that take up “36% of the out-of-core part” in the Polimi and TUDelft models [9]. Most of the cooling happens in the top half of the heat exchanger where the temperature differential between the primary and intermediate loops is the largest. In the Polimi and TUDelft models, the overall  $h$  is the “harmonic mean of the heat transfer coefficients on each side of the heat exchanger”. For this loss of flow transient, the authors intended to focus on the primary loop and assumed that only the pumps in the primary loop failed. In addition to this, the authors applied the Dittus-Boelter correlation [57] for the relationship between the primary side  $h$  and  $\dot{m}$ . The Dittus-Boelter correlation for fluids being cooled is:

$$Nu = 0.023Re^{0.8}Pr^{0.3} \quad (6.2)$$

where

$Nu$  = Nusselt number,

$Re$  = Reynolds number,

$Pr$  = Prandtl number.

The only direct relation to  $\dot{m}$  in the Dittus-Boelter correlation is through the  $Re$  term, which is directly proportional to flow velocity  $v$ . This gives the following relation between  $h$  and  $v$ :

$$h \propto v^{0.8} \quad (6.3)$$

However, this relation provided very different results in the unprotected loss of flow and pump overspeed transients compared with the Polimi and TUDelft models; it overpredicted the equilibrium power output in the unprotected loss of flow transient and underpredicted the same parameter in the unprotected pump overspeed transient. Upon further investigation, the present author found that raising the power of  $v$  from 0.8 to 1.1 brought the average core temperatures closer to the results from the other models in both transients. Therefore, this work adopted the raised power in this study.

Another issue pertained to the turbulent viscosity  $\mu_t$  as a function of  $v$ . Using a simple approximation of  $\mu_t$  being directly proportional to  $v$ , the results differed significantly compared with the Polimi and TUDelft models. This is likely due to buoyancy-driven flow contributing to turbulence; the turbulent energy  $k$  equation in COMSOL's  $k$ - $\epsilon$  model has an explicit source term from buoyancy effects [58]. Another point to note is the Reynolds number remains constant if  $\mu$  and  $v$  decrease in tandem. This preserves the existence of the recirculation zone in the core and it is at odds with the results from the Polimi and TUDelft models, which show that the recirculation zones disappear during the loss of flow transient. We circumvented this issue by letting fixed fractions of the initial  $\mu_{t,0}$  be conserved regardless of the final flow velocity, according to the following equation:

$$\mu_t = \mu_c + (\mu_{t,0} - \mu_c)e^{-t/8} \quad (6.4)$$

where

$$\mu_c = \text{conserved fraction of } \mu_{t,0} \text{ [Pa}\cdot\text{s]}.$$

This measure allowed for laminar flow to develop in the core and yielded results with closer resemblance to those from the Polimi and TUDelft models.

Figures 6.9 and 6.10 show the power output and average core temperature increase during the unprotected loss of flow transient in the Moltres, Polimi, and TUDelft models without decay heat modeling. The three sets of results from Moltres correspond to  $\mu_c = \frac{1}{4}\mu_{t,0}$ ,  $\frac{1}{2}\mu_{t,0}$ , and  $\frac{3}{4}\mu_{t,0}$ . Moltres performs poorer in this transient relative to the two previous transients. Although Moltres shows the same decreasing trend in power output, it failed to capture the exact individual features in the reactor response. In the Polimi and TUDelft models, Fiorina et al. stated that after around  $t = 15$  s, the “flow pattern changed in the core and the recirculation zones started to disappear”. A sudden drop in the average core temperature results as the pocket of hot salt leaves the core. In Moltres, the wider peak in the average core temperature indicates that there was a more gradual change in the flow pattern.

Figure 6.11 shows the flow patterns and temperature distribution in the core at  $t = 300$  s in all three models. Figures 6.9, 6.10, and 6.11 combined highlight the difference between laminar flow in

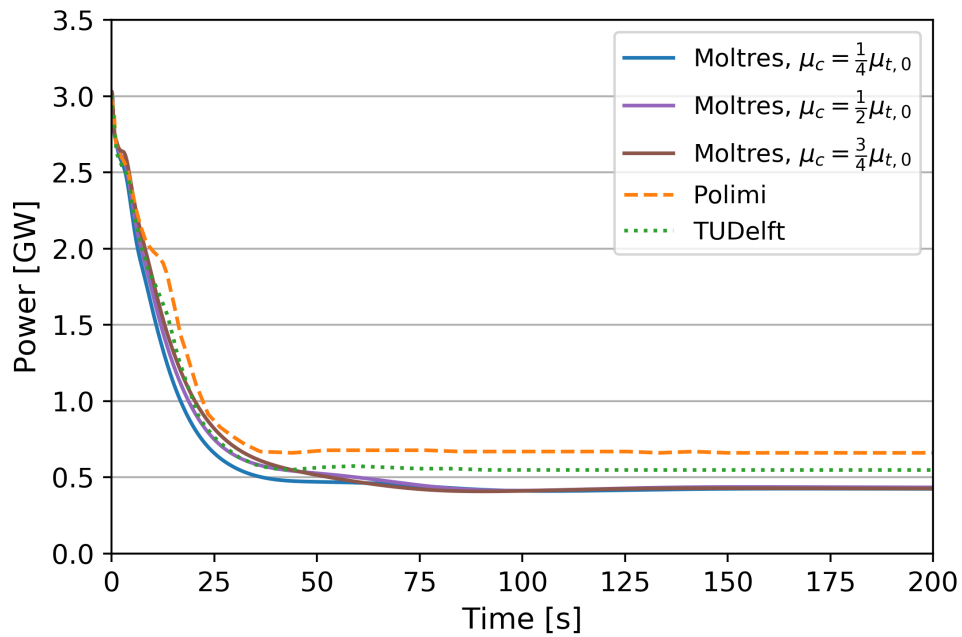


Figure 6.9: Power output during an unprotected loss of flow transient in the Moltres, Polimi, and TUDelft models [9].

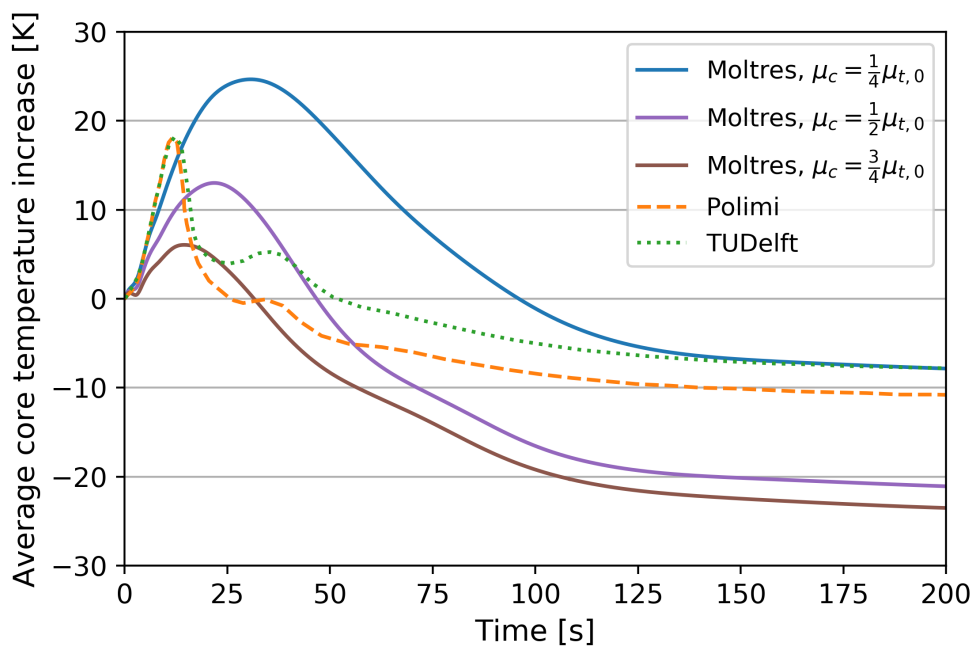


Figure 6.10: Average core temperature increase during an unprotected loss of flow transient in the Moltres, Polimi, and TUDelft models [9].

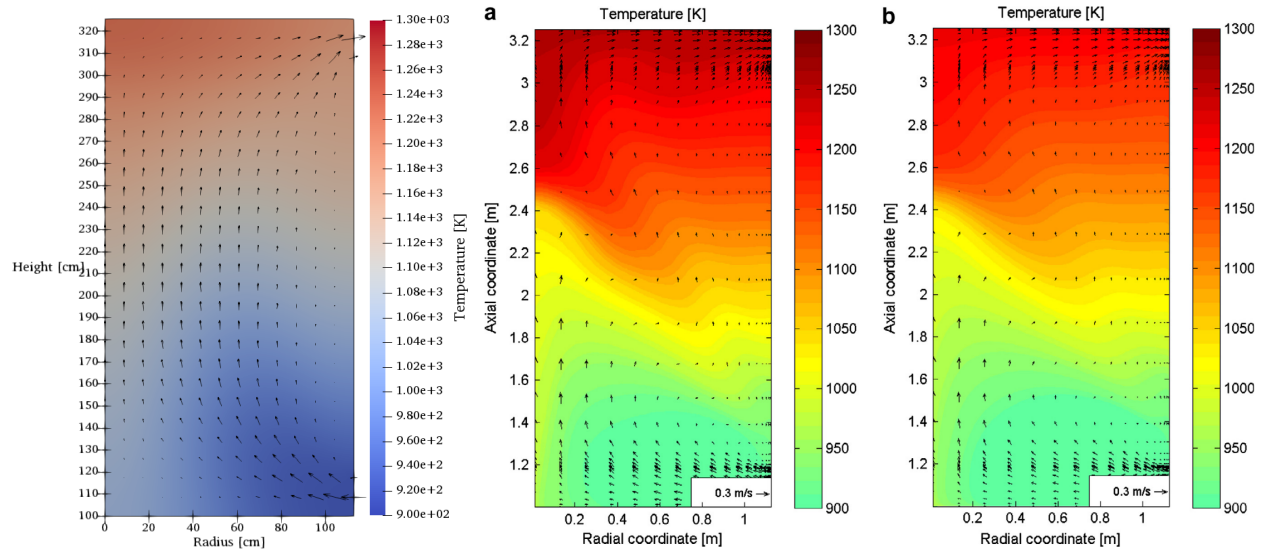


Figure 6.11: Temperature and velocity fields in the core at  $t = 300$  s during a loss of flow transient in the Moltres ( $\mu_c = \frac{1}{2}\mu_{t,0}$ ), Polimi, and TUDelft models.

the Moltres model and buoyancy-driven flow in the other models, and its impact on the reactor response. They show that low-speed laminar flow is a poor substitute for buoyancy-driven flow in the context of the MSFR. It is particularly evident in the transition from high-speed turbulent flow to low-speed viscous flow as Moltres mispredicted the intermediate stages. The simplifying assumption for the uniform, time-dependent  $\mu_t$  is also flawed in a safety analysis code.

The results from this transient inform our goals for Moltres: 1) implementing a proper turbulence model, and 2) developing a new heat exchanger feature that is compatible with the buoyancy-driven flow capabilities already present in Moltres.

## 6.4 Unprotected Pump Overspeed

Pump overspeed refers to a sustained increase in pump speed in the primary coolant loop. The increased flow rate  $\dot{m}$  impacts reactor performance in several ways. It affects the neutronics by reducing the in-core  $\beta$  as more of the shorter-lived precursors will tend to flow out of the core before decaying. This net loss of neutrons reduces the reactivity in the core, thereby causing core temperatures to fall to counteract this change through temperature reactivity feedback. The increased  $\dot{m}$  also enhances the heat transfer coefficient on the primary loop side of the heat exchanger and enables the reactor to operate at a higher power output. At the same time, the improved mixing flattens the temperature distribution in the core.

This work followed Fiorina et al.'s implementation [9] by ramping up the inlet velocity,  $u$ , by 50% from the nominal value,  $u_0$ , according to the following formula:

$$u(t) = u_0[1 + 0.5(1 - e^{-t/\tau})] \quad (6.5)$$

where

$$\tau = 5 \text{ s.}$$

For this transient, this work assumed that  $\mu_t$  was directly proportional to  $v$  because the buoyancy effects are negligible and the recirculation zones persist throughout the entire duration. Figures 6.12 and 6.13 show the power output and average core temperature increase during the unprotected pump overspeed transient in the Moltres, Polimi, and TUDelft models. Figure 6.14 shows the same results for the first 20 seconds of the transient. At the start of the transient, the rising flow rate cools the core and causes power output to rise sharply. Although the average core temperature has a strictly decreasing trend, the temperature at the center of the core briefly rises due to the sharp increase in power output. Since this is the region where most of the fissions take place, the Doppler effect and salt expansion causes the power output to stall and dip briefly before rising again at  $t = 2.5$  s. The reactor tends to a new equilibrium power output and average core temperature. The temperature distribution in the core is more evenly distributed because the turbulent thermal

conductivity  $k_t$  is directly proportional to  $mu_t$ .

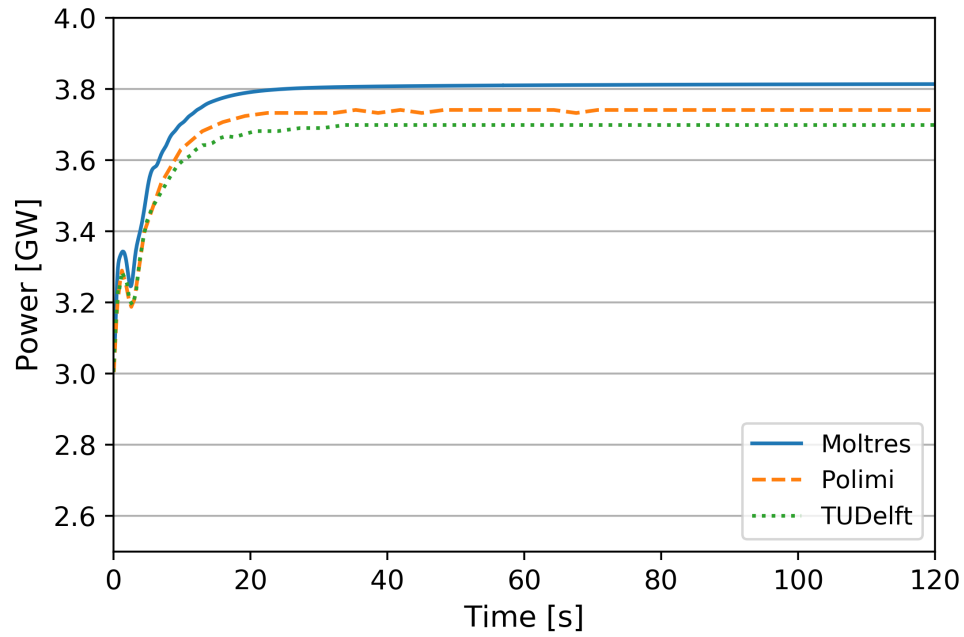


Figure 6.12: Power output during an unprotected pump overspeed transient in the Moltres, Polimi, and TUDelft models [9].

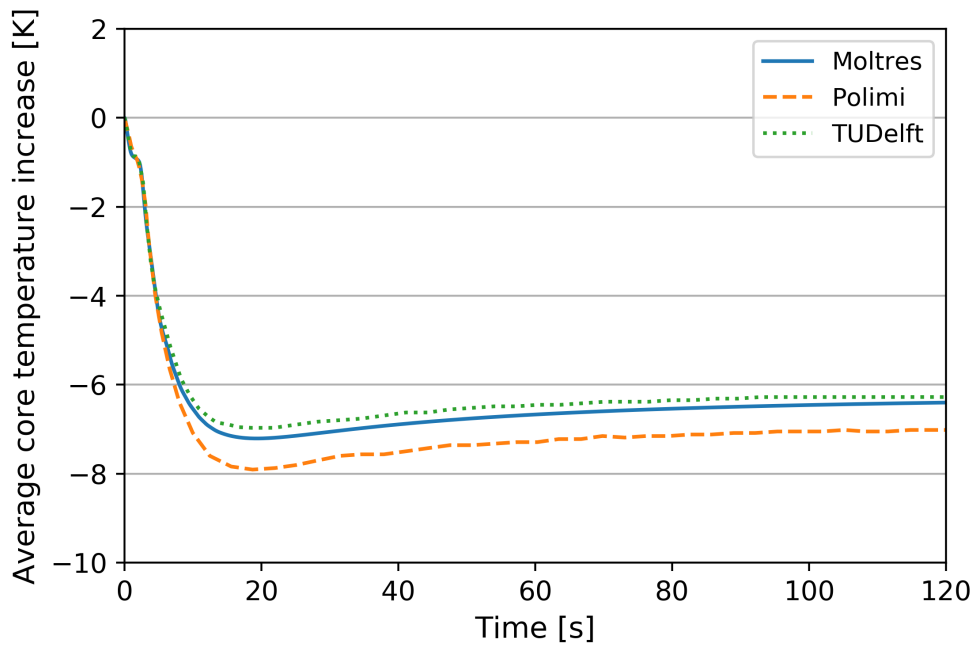


Figure 6.13: Average core temperature increase during an unprotected pump overspeed transient in the Moltres, Polimi, and TUDelft models [9].

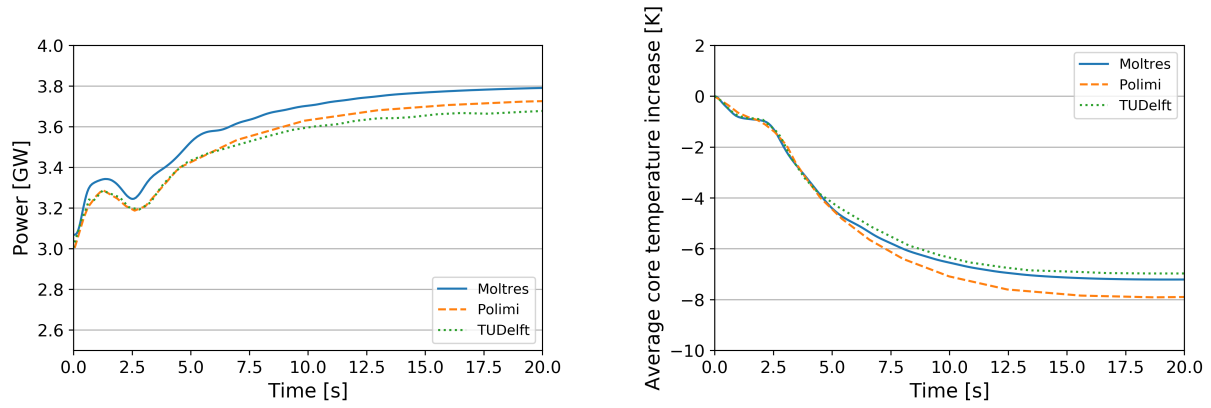


Figure 6.14: The first 20 s of the power output and average core temperature increase during an unprotected pump overspeed transient.

The results show excellent agreement with the Polimi and TUDelft models. The average core temperature increase in particular reproduces the Polimi and TUDelft results very well and the curve falls between the other two curves. The power output is higher because the Moltres MSFR model has a stronger negative temperature coefficient than the other two models.



# Chapter 7

## Conclusion

The unique phenomena in MSRs necessitate the development of new reactor safety analysis software. This thesis presents the latest developments in Moltres, namely coupling its existing neutron diffusion module to the incompressible Navier-Stokes module in MOOSE, and developing a decay heat model for short-term transients. We demonstrated and verified some of its current capabilities through a static neutronics study, and a coupled neutronics/thermal-hydraulics safety analysis of the MSFR concept.

The neutronics study showed good agreement between Moltres and Serpent. With the relevant group constant data from Serpent, Moltres could accurately replicate the  $k_{eff}$ ,  $\beta$ ,  $\alpha_T$ , and multi-group neutron flux results from Serpent. The  $k_{eff}$  estimates from Moltres were approximately 100 pcm higher for all measurements between 800 K and 1400 K. This discrepancy is notably smaller than the discrepancies observed in the neutron diffusion and SP3 models developed in OpenFOAM [53]. The  $\beta$  and  $\alpha_T$  values from Moltres had 1.46% and 0.265% discrepancies, respectively, to Serpent's results. Lastly, the normalized six-group neutron flux from Moltres and Serpent were visually indistinguishable from each other. The journal article that introduced Moltres [11] verified its neutron diffusion model for a two-group thermal-spectrum MSBR model; the results of this study extends code-to-code verification of Moltres' neutron diffusion model with the six-group, fast-spectrum MSFR model.

Although Moltres currently lacks a proper turbulence model, our simplifying assumption for the turbulent viscosity  $\mu_t$  yielded good results for most of the MSFR steady-state and transient analyses. The steady-state temperature and velocity distributions showed many similarities in their shapes and magnitudes to the Polimi and TUDelft model results [9]. Our uniform  $\mu_t$  assumption accounted for the minor differences in the flow at the top of the core and the loss of delayed neutrons to out-of-core emissions. The results with the decay heat model showed a slight flattening of the

temperature distribution in the core that is in line with our expectations given the diffusion and advection of the decay heat precursors.

The unprotected reactivity insertion and loss of heat sink results showed the same trends Fiorina et al. observed in their Polimi and TUDelft models. The small difference in the temperature reactivity coefficient accounted for the small difference in the magnitude of the peaks in power output and average core temperature increase. The differences between the pointwise heat exchanger in Moltres and the volumetric heat exchanger in the other two models required minor adjustments in the relationship between flow rate  $\dot{m}$  and the heat transfer coefficient  $h$  from the original Dittus-Boelter correlation for the pump-initiated transients. Assuming a directly proportional relationship between  $\mu_t$  and  $\dot{m}$  yielded results in good agreement with the other two models for the pump overspeed transient. However, Moltres performed poorly in the loss of flow transient as this work could not incorporate buoyancy-driven flow and its associated effects on  $\mu_t$ .

Overall, we have demonstrated that Moltres can handle most of the case studies that this thesis covered.

## 7.1 Future Work

Further research and development on Moltres should aim to rectify the issues mentioned in this thesis. This work has highlighted three main avenues for improvement. Firstly, proper 2D/3D heat exchanger implementation would allow us to move away from the 1D outer loop system and towards a full 2D/3D closed loop. The biggest change is that users would be able to use the Boussinesq approximation for buoyancy-driven flow capability in Moltres. Buoyancy-driven flow is a critical component in loss of forced flow scenarios and these scenarios in turn are important accident transients in reactor safety analyses.

Secondly, Moltres would benefit from a proper turbulence model such as the  $k$ - $\epsilon$  or  $k$ - $\omega$  turbulence models. Turbulence effects are significant in MSR designs with fast flow, and they inform optimization studies for improving flow patterns and eliminating local hotspots in eddies. Our work in this thesis, particularly for the loss of flow transient, shows that simplifying assumptions for turbulence lead to erroneous results under flow conditions that deviate significantly from steady state.

Lastly, a compressible Navier-Stokes model would be essential for modeling compressible flow

effects such as variable temperature-dependent density changes following a large reactivity insertion and finite wave propagation speeds in a fluid. The presence of bubbles in the core from the gas sparging system increases fuel compressibility and enhances compressibility effects [54].

# References

- [1] N. US Department of Commerce, “Global Monitoring Laboratory - Carbon Cycle Greenhouse Gases,” 2020. Library Catalog: [www.esrl.noaa.gov](http://www.esrl.noaa.gov).
- [2] A. J. McMichael, D. Campbell-Lendrum, S. Kovats, S. Edwards, P. Wilkinson, T. Wilson, R. Nicholls, S. Hales, F. Tanser, D. Le Sueur, M. Schlesinger, and N. Andronova, “Global Climate Change (Chapter 20),” in *Comparative Quantification of Health Risks*, pp. 1543–1649, World Health Organization, 2004. Library Catalog: [www.unscn.org](http://www.unscn.org).
- [3] IEA, “Global Energy and CO2 Status Report 2018,” tech. rep., International Energy Agency, Paris, France, Mar. 2019.
- [4] D. Petti, “The Future of Nuclear Energy in a Carbon-Constrained World,” *Massachusetts Institute of Technology Energy Initiative (MITEI)*, p. 272, 2018.
- [5] Massachusetts Institute of Technology, *The Future of nuclear power: an interdisciplinary MIT Study*. Boston MA: MIT, 2003. OCLC: 53208528.
- [6] GIF, “A technology roadmap for generation IV nuclear energy systems,” Tech. Rep. GIF-002-00, US DOE Nuclear Energy Research Advisory Committee and the Generation IV International Forum, 2002.
- [7] E. E. Pettersen and K. Mikityuk, “Coupled multi-physics simulations of the Molten Salt Fast Reactor using coarse-mesh thermal-hydraulics and spatial neutronics,” Master’s thesis, MSc thesis, September 2016 (PDF), 2016.
- [8] A. O. Graham, B. S. O. Collins, R. O. Salko Jr, R. Z. Taylor, and C. A. O. Gentry, “Development of Molten Salt Reactor Modeling and Simulation Capabilities in VERA,” tech. rep., Oak Ridge National Lab. (ORNL), Oak Ridge, TN (United States), Sept. 2019.
- [9] C. Fiorina, D. Lathouwers, M. Aufiero, A. Cammi, C. Guerrieri, J. L. Kloosterman, L. Luzzi, and M. E. Ricotti, “Modelling and analysis of the MSFR transient behaviour,” *Annals of Nuclear Energy*, vol. 64, pp. 485–498, Feb. 2014.
- [10] M. Aufiero, A. Cammi, O. Geoffroy, M. Losa, L. Luzzi, M. E. Ricotti, and H. Rouch, “Development of an OpenFOAM model for the Molten Salt Fast Reactor transient analysis,” *Chemical Engineering Science*, vol. 111, pp. 390–401, May 2014.
- [11] A. Lindsay, G. Ridley, A. Rykhlevskii, and K. Huff, “Introduction to Moltres: An application for simulation of Molten Salt Reactors,” *Annals of Nuclear Energy*, vol. 114, pp. 530–540, Apr. 2018.

- [12] D. R. Gaston, C. J. Permann, J. W. Peterson, A. E. Slaughter, D. Andr, Y. Wang, M. P. Short, D. M. Perez, M. R. Tonks, J. Ortensi, L. Zou, and R. C. Martineau, “Physics-based multiscale coupling for full core nuclear reactor simulation,” *Annals of Nuclear Energy*, vol. 84, pp. 45–54, Oct. 2015.
- [13] M. W. Rosenthal, P. R. Kasten, and R. B. Briggs, “Molten-Salt Reactors - History, Status, and Potential,” *Nuclear Applications and Technology*, vol. 8, pp. 107–117, Feb. 1970.
- [14] P. N. Haubenreich and J. R. Engel, “Experience with the Molten-Salt Reactor Experiment,” *Nuclear Technology*, vol. 8, pp. 118–136, Feb. 1970.
- [15] H. G. MacPherson, “The Molten Salt Reactor Adventure,” *Nuclear Science and Engineering*, vol. 90, pp. 374–380, Aug. 1985.
- [16] J. C. Gehin and J. J. Powers, “Liquid Fuel Molten Salt Reactors for Thorium Utilization,” *Nuclear Technology*, vol. 194, pp. 152–161, May 2016.
- [17] J. Smith and W. E. Simmons, “An assessment of a 2500 MWe molten chloride salt fast reactor,” Tech. Rep. AEEW-R956, United Kindom Atomic Energy Authority, Aug. 1974.
- [18] D. LeBlanc, “Integral molten salt reactor,” Feb. 2015.
- [19] Transatomic Power Corporation, “Technical White Paper,” White Paper 2.1, Transatomic Power Corporation, Cambridge, MA, United States, Nov. 2016.
- [20] J. Serp, M. Allibert, O. Benes, S. Delpech, O. Feynberg, V. Ghetta, D. Heuer, D. Holcomb, V. Ignatiev, J. L. Kloosterman, L. Luzzi, E. Merle-Lucotte, J. Uhl, R. Yoshioka, and D. Zhimin, “The molten salt reactor (MSR) in generation IV: Overview and perspectives,” *Progress in Nuclear Energy*, vol. 77, pp. 308–319, Nov. 2014.
- [21] V. Ignatiev, O. Feynberg, I. Gnidoi, A. Merzlyakov, A. Surenkov, V. Uglov, A. Zagnitko, V. Subbotin, I. Sannikov, A. Toropov, V. Afonichkin, A. Bovet, V. Khokhlov, V. Shishkin, M. Kormilitsyn, A. Lizin, and A. Osipenko, “Molten salt actinide recycler and transforming system without and with Th-U support: Fuel cycle flexibility and key material properties,” *Annals of Nuclear Energy*, vol. 64, pp. 408–420, Feb. 2014.
- [22] A. Rykhlevskii, J. W. Bae, and K. D. Huff, “Modeling and simulation of online reprocessing in the thorium-fueled molten salt breeder reactor,” *Annals of Nuclear Energy*, vol. 128, pp. 366–379, June 2019.
- [23] B. M. Elsheikh, “Safety assessment of molten salt reactors in comparison with light water reactors,” *Journal of Radiation Research and Applied Sciences*, vol. 6, pp. 63–70, Oct. 2013.
- [24] I. K. Aji, T. Tatsuya, M. Kinoshita, and T. Okawa, “An Experimental and Numerical Study of Wall Effect on Freeze Valve Performance in a Molten Salt Reactor,” *Journal of Nuclear Engineering and Radiation Science*, vol. 6, Apr. 2020.
- [25] M. Brovchenko, D. Heuer, E. Merle, M. Allibert, V. Ghetta, A. Laureau, and P. Rubiolo, “Design-Related Studies for the Preliminary Safety Assessment of the Molten Salt Fast Reactor,” *Nuclear Science and Engineering*, vol. 175, pp. 329–339, Nov. 2013.
- [26] R. Yoshioka, M. Kinoshita, and I. Scott, “7 - Materials,” in *Molten Salt Reactors and Thorium Energy* (T. J. Dolan, ed.), pp. 189–207, Woodhead Publishing, 2017.

- [27] M. K. M. Ho, G. H. Yeoh, and G. Braoudakis, “Molten salt reactors,” in *Materials and processes for energy: communicating current research and technological developments* (A. Mndez-Vilas, ed.), no. 1 in Energy Book Series, pp. 761–768, Badajoz, Spain: Formatex Research Center, 2013 ed., 2013. <http://www.formatex.info/energymaterialsbook/>  
<http://www.energymaterialsbook.org/chapters.html>.
- [28] T. Kamei, “Recent Research of Thorium Molten-Salt Reactor from a Sustainability Viewpoint,” *Sustainability*, vol. 4, pp. 2399–2418, Sept. 2012.
- [29] E. Merle-Lucotte, D. Heuer, M. Allibert, M. Brovchenko, N. Capellan, and V. Ghetta, “Launching the thorium fuel cycle with the Molten Salt Fast Reactor,” in *Proceedings of ICAPP*, pp. 2–5, 2011.
- [30] S. Grape and C. Hellesen, “10 - Nonproliferation and safeguards aspects of the MSR fuel cycle,” in *Molten Salt Reactors and Thorium Energy* (T. J. Dolan, ed.), pp. 261–279, Woodhead Publishing, 2017.
- [31] T. J. Dolan, “1 - Introduction,” in *Molten Salt Reactors and Thorium Energy*, pp. 1–12, Woodhead Publishing, 2017.
- [32] R. Moir, “Recommendations for a restart of molten salt reactor development,” *Energy Conversion and Management*, vol. 49, pp. 1849–1858, July 2008.
- [33] J. Krepel, U. Rohde, U. Grundmann, and F.-P. Weiss, “DYN3D-MSR spatial dynamics code for molten salt reactors,” *Annals of Nuclear Energy*, vol. 34, pp. 449–462, June 2007.
- [34] J. Kophazi, D. Lathouwers, and J. Kloosterman, “Development of a Three-Dimensional Time-Dependent Calculation Scheme for Molten Salt Reactors and Validation of the Measurement Data of the Molten Salt Reactor Experiment,” *Nuclear Science and Engineering*, vol. 163, no. 2, pp. 118–131, 2009.
- [35] A. Cammi, V. Di Marcello, L. Luzzi, V. Memoli, and M. E. Ricotti, “A multi-physics modelling approach to the dynamics of Molten Salt Reactors,” *Annals of Nuclear Energy*, vol. 38, pp. 1356–1372, June 2011.
- [36] M. Zanetti, A. Cammi, C. Fiorina, and L. Luzzi, “A Geometric Multiscale modelling approach to the analysis of MSR plant dynamics,” *Progress in Nuclear Energy*, vol. 83, pp. 82–98, Aug. 2015.
- [37] A. Laureau, D. Heuer, E. Merle-Lucotte, P. R. Rubiolo, M. Allibert, and M. Aufiero, “Transient coupled calculations of the Molten Salt Fast Reactor using the Transient Fission Matrix approach,” *Nuclear Engineering and Design*, vol. 316, pp. 112–124, May 2017.
- [38] L. Mathieu, D. Heuer, R. Brissot, C. Garzenne, C. Le Brun, D. Lecarpentier, E. Liatard, J.-M. Loiseaux, O. Mplan, E. Merle-Lucotte, A. Nuttin, E. Walle, and J. Wilson, “The thorium molten salt reactor: Moving on from the MSBR,” *Progress in Nuclear Energy*, vol. 48, pp. 664–679, Sept. 2006.
- [39] E. Merle, D. Heuer, M. Allibert, V. Ghetta, C. Brun, L. Mathieu, R. Brissot, and E. Liatard, “Optimized transition from the reactors of second and third generations to the Thorium Molten Salt Reactor,” May 2007.

- [40] M. Brovchenko, J.-L. Kloosterman, L. Luzzi, E. Merle, D. Heuer, A. Laureau, O. Feynberg, V. Ignatiev, M. Aufiero, A. Cammi, C. Fiorina, F. Alcaro, S. Dulla, P. Ravetto, L. Frima, D. Lathouwers, and B. Merk, “Neutronic benchmark of the molten salt fast reactor in the frame of the EVOL and MARS collaborative projects,” *EPJ Nuclear Sciences & Technologies*, vol. 5, p. 2, Jan. 2019.
- [41] EURATOM, “Final Report Summary - EVOL (Evaluation and Viability of Liquid Fuel Fast Reactor System) | Report Summary | EVOL | FP7| European Commission,” Final report 249696, EURATOM, France, 2015.
- [42] E. Merle, “Concept of Molten Salt Fast Reactor,” 2017.
- [43] J. Leppanen, M. Pusa, T. Viitanen, V. Valtavirta, and T. Kaltiaisenaho, “The Serpent Monte Carlo code: Status, development and applications in 2013,” *Annals of Nuclear Energy*, vol. 82, pp. 142–150, Aug. 2014.
- [44] “Trelis (Version 16.5),” 2018.
- [45] M. B. Chadwick, “ENDF/B-VII.1 Nuclear Data for Science and Technology: Cross Sections, Covariances, Fission Product Yields and Decay Data,” *Nuclear Data Sheets*, vol. 112, pp. 2887–2996, Dec. 2011.
- [46] OECD/NEA, “The JEFF-3.1.2 Nuclear Data Library,” Tech. Rep. JEFF Report 24, OECD/NEA Data Bank, OECD/NEA, 2014.
- [47] A. Lindsay, “Moltres, software for simulating Molten Salt Reactors,” 2017. <https://github.com/arfc/moltres>.
- [48] B. S. Kirk, J. W. Peterson, R. H. Stogner, and G. F. Carey, “libMesh: a C++ library for parallel adaptive mesh refinement/coarsening simulations,” *Engineering with Computers*, vol. 22, pp. 237–254, Dec. 2006.
- [49] B. Satish, A. Shrirang, M. F. Adams, J. Brown, P. Brune, K. Buschelman, L. Dalcin, A. Dener, V. Eijkhout, W. D. Gropp, D. Karpeyev, D. Kaushik, M. G. Knepley, D. A. May, L. C. McInnes, R. T. Mills, T. Munson, K. Rupp, P. Sanan, B. F. Smith, S. Zampini, and H. Zhang, “PETSc Users Manual,” Tech. Rep. ANL-95/11 - Revision 3.12, Argonne National Laboratory, 2019.
- [50] J. W. Peterson, A. D. Lindsay, and F. Kong, “Overview of the Incompressible Navier-Stokes simulation capabilities in the MOOSE Framework,” *arXiv:1710.08898 [math]*, Oct. 2017. arXiv: 1710.08898.
- [51] S. M. Park, A. Rykhlevskii, and K. Huff, “Safety Analysis of Molten Salt Fast Reactor Fuel Composition using Moltres,” in *Proceedings of GLOBAL International Fuel Cycle Conference*, (Seattle, WA, United States), American Nuclear Society, Sept. 2019.
- [52] Y. Bartosiewicz and M. Duponcheel, “6.1.2 - Large-eddy simulation: Application to liquid metal fluid flow and heat transfer,” in *Thermal Hydraulics Aspects of Liquid Metal Cooled Nuclear Reactors* (F. Roelofs, ed.), pp. 245–271, Woodhead Publishing, Jan. 2019.
- [53] M. Aufiero, A. Cammi, C. Fiorina, J. Leppnen, L. Luzzi, and M. E. Ricotti, “An extended version of the SERPENT-2 code to investigate fuel burn-up and core material evolution of the Molten Salt Fast Reactor,” *Journal of Nuclear Materials*, vol. 441, pp. 473–486, Oct. 2013.

- [54] E. Cervi, S. Lorenzi, A. Cammi, and L. Luzzi, “Development of a multiphysics model for the study of fuel compressibility effects in the Molten Salt Fast Reactor,” *Chemical Engineering Science*, vol. 193, pp. 379–393, Jan. 2019.
- [55] H. Rouch, O. Geoffroy, P. Rubiolo, A. Laureau, M. Brovchenko, D. Heuer, and E. Merle-Lucotte, “Preliminary thermalhydraulic core design of the Molten Salt Fast Reactor (MSFR),” *Annals of Nuclear Energy*, vol. 64, pp. 449–456, Feb. 2014.
- [56] C. Fiorina, *The molten salt fast reactor as a fast spectrum candidate for thorium implementation*. PhD, Politecnico Di Milano, Mar. 2013.
- [57] F. W. Dittus and L. M. K. Boelter, “Heat transfer in automobile radiators of the tubular type,” *University of California Publications in Engineering*, vol. 2, pp. 443–461, Oct. 1930.
- [58] C. AB, “COMSOL Multiphysics,” 2018.